














Light curves of transneptunian objects from the K2 mission of the Kepler Space Telescope

VIKTÓRIA KECSKEMÉTHY ^{1,2,3} CSABA KISS ^{1,2,4} RÓBERT SZAKÁTS ^{1,2} ANDRÁS PÁL ^{1,2,5} GYULA M. SZABÓ ^{6,7}
LÁSZLÓ MOLNÁR ^{1,2,4,8} KRISZTIÁN SÁRNECZKY ^{1,2} JÓZSEF VINKÓ ^{1,2,4} RÓBERT SZABÓ ^{1,2,4,8}
GÁBOR MARTON ^{1,2} ANIKÓ FARKAS-TAKÁCS ^{1,2,5} CSILLA E. KALUP ^{1,2,5} AND LÁSZLÓ L. KISS ^{1,2,9}

¹*Konkoly Observatory, Research Centre for Astronomy and Earth Sciences, Eötvös Loránd Research Network, Konkoly Thege Miklós út 15-17, H-1121 Budapest, Hungary*

²*CSFK, MTA Centre of Excellence, Budapest, Konkoly Thege Miklós út 15-17, H-1121, Hungary*

³*Leiden Observatory, Leiden University, Niels Bohrweg 2, 2333 CA Leiden, The Netherlands*

⁴*Eötvös Loránd University, Institute of Physics, Pázmány Péter sétány 1/A, H-1171 Budapest, Hungary*

⁵*Eötvös Loránd University, Faculty of Science, Pázmány Péter sétány 1/A, H-1171 Budapest, Hungary*

⁶*ELTE Eötvös Loránd University, Gothard Astrophysical Observatory, Szombathely, Hungary*

⁷*MTA-ELTE Exoplanet Research Group, 9700 Szombathely, Szent Imre h. u. 112, Hungary*

⁸*MTA CSFK Lendület Near-Field Cosmology Research Group*

⁹*Sydney Institute for Astronomy, School of Physics A29, University of Sydney, NSW 2006, Australia*

(Received October 14, 2022; Revised October 14, 2022; Accepted October 14, 2022)

Submitted to ApJS

ABSTRACT

The K2 mission of the Kepler Space Telescope allowed the observations of light curves of small solar system bodies throughout the whole Solar system. In this paper we present the results of a collection of K2 transneptunian object observations, between Campaigns C03 (November 2014 – February 2015) to C19 (August – September, 2018), which includes 66 targets. Due to the faintness of our targets the detectability rate of a light curve period is $\sim 56\%$, notably lower than in the case of other small body populations, like Hildas or Jovian trojans. We managed to obtain light curve periods with an acceptable confidence for 37 targets; the majority of these cases are new identifications. We were able to give light curve amplitude upper limits for the other 29 targets. Several of the newly detected light curve periods are longer than ~ 24 h, in many cases close to ~ 80 h, i.e., these targets are slow rotators. This relative abundance of slowly rotating objects is similar to that observed among Hildas, Jovian trojans and Centaurs in the K2 mission, and also among main belt asteroids measured with the TESS Space Telescope. Transneptunian objects show notably higher light curve amplitudes at large ($D \gtrsim 300$ km) sizes than that found among large main belt asteroids, in contrast to the general expectation that due to their lower compressive strength they reach hydrostatic equilibrium at smaller sizes than their inner solar system counterparts.

Keywords: Light curves (918) – trans-Neptunian Objects (1705)

1. INTRODUCTION

Despite almost three decades of observations the number of trans-Neptunian objects (TNOs) with known rotational properties – at least rotation period and light curve amplitude – is still rather low. While amplitude

estimates exist for a larger number of objects (see e.g. Showalter et al. 2021), the latest version of the Light Curve Database (LCDB, Warner et al. 2009) contains only 124 TNOs with known rotation periods. In many cases, even these periods are not very reliable, and different authors derive different solutions based on their own data (see e.g. Sheppard et al. 2008; Duffard et al. 2009; Thirouin et al. 2014).

Light curves hold information on the formation and evolution of individual objects and on the collisional evolution of the asteroid populations. In the main belt large, $D \geq 40$ km asteroids have likely reached collisional equilibrium and the corresponding Maxwellian spin frequency distribution, while the rotation of smaller asteroids are modified by non-collisional and non-gravitational effects as well (see e.g. Pravec et al. 2002, and references therein). In the transneptunian region smaller bodies with diameters $D \leq 100$ km are likely collisional fragments with their rotation states erased and heavily overwritten, while intermediate sized objects ($100 \text{ km} \leq D \leq 200 \text{ km}$) have probably been stable to catastrophic breakups, but their spin states are likely strongly influenced by impacts. On the other hand, the largest objects ($D \geq 200 \text{ km}$) likely kept their spin states inherited from the formation era in the early Solar system (see Sheppard et al. 2008, and references therein).

Binaries, especially contact and semi-contact systems, however, may alter this picture significantly, as they may end up in fully synchronised spin-orbit states (Noll et al. 2020) or become collapsed binaries (Nesvorný et al. 2020) at the end of their tidal evolution, potentially increasing the number of slow rotators (Marton et al. 2020). While there are a large number of minor planets with known light curves below the collisional decoupling limit in the main belt or in the Hilda and Jovian trojan populations, the vast majority of TNOs with known rotational characteristics are larger than ~ 100 km. This means that their rotational properties are expected to be chiefly determined by their formation circumstances and/or by their tidal evolution in multiple systems.

Earlier reviews of transneptunian light curves reported mean rotation periods of $P = 7\text{--}8$ h (e.g. Dufard et al. 2009), however, it was also found that the binary transneptunian population rotates slower (Thirouin et al. 2014), and objects in the cold classical population have larger variability and rotate slower than the non-cold classical TNOs (Benecchi & Sheppard 2013a; Thirouin & Sheppard 2019a). In the latter case the mean rotation rates were within the uncertainties, $P = 9.47 \pm 1.53$ h, and $P = 8.45 \pm 0.58$ h, respectively, for the two samples. In the case of Centaurs – which are believed to be originated from the transneptunian region – Marton et al. (2020) identified several targets with long, $P \geq 20$ h rotation periods, indicating that the previous ground-based light curve samples might have missed slowly rotating objects.

While ground-based observations have obvious limitations in detecting long-period light curves (see e.g. Marciniak et al. 2015, 2018), the K2 mission of the Kepler Space Telescope (Howell et al. 2014) allowed

long (up to ~ 80 days), uninterrupted observations of many Solar system objects, including main belt asteroids (Szabó et al. 2015, 2016; Molnár et al. 2018), Hildas (Szabó et al. 2020), Jovian trojans (Szabó et al. 2017; Ryan et al. 2017; Kalup et al. 2021), and also the irregular satellites of giant planets (Kiss et al. 2016; Farkas-Takács et al. 2017). Light curves were also published for a few, selected transneptunian objects based on K2 observations (Pál et al. 2015, 2016). A common outcome of the studies of larger samples, across all dynamical classes, was the identification of an increased number of targets with long rotation periods compared to previous ground-based studies. A similar trend is observed among the data of nearly 10 000 main belt asteroids obtained by the TESS Space Telescope (Pál et al. 2020), and asteroids with long rotation periods were identified in other surveys like the Asteroid Terrestrial-impact Last Alert System (ATLAS), the Zwicky Transient Facility (ZTF, Erasmus et al. 2021), and the All-Sky Automated Survey for Supernovae (ASAS-SN, Hanuš et al. 2021).

In this paper we present the analysis of light curve data for 66 transneptunian objects obtained by the K2 mission of the Kepler Space Telescope. The observations and the main data reduction steps are summarised in Sect. 2, results and comparison with the light curve characteristics of other populations and datasets are presented in Sect. 3, and conclusions are given in Sect. 4. Large tables of observational data, light curve figures, and the description of electronically available light curve data can be found in the Appendix.

2. OBSERVATIONS AND DATA REDUCTION

2.1. Basic data reduction

The Kepler Space Telescope observed numerous Solar System objects during the K2 mission. The observing strategy and data reduction steps followed in this paper are analogous to other TNO, Centaur and asteroid targets published in previous papers (see Kiss et al. 2020, for a summary). Since *Kepler* observed only selected pixels during each 60–80 d long campaign, pixels over ~ 30 d long arcs of the apparent trajectories were allocated for each target. We processed the *Kepler* observations with the *fitsh* software package (Pál 2012). First, we assembled the individual Target Pixel Files of both the track of the target and that of the nearby stars into mosaic images. Astrometric solutions were derived for every mosaic frame in the campaign, using the Full Frame Images (acquired once per campaign) as initial hints, and the frames were registered into the same reference system. We then enlarged the images by roughly 3 times, and rotated them into RA-Dec direc-

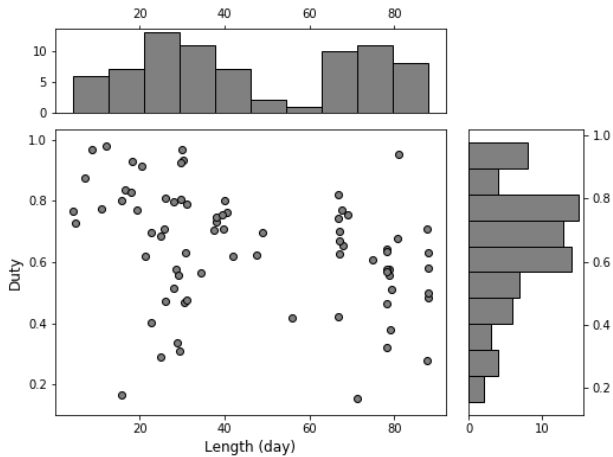


Figure 1. Duty cycle versus the full length of the observations. Histograms of duty cycle and observation length are shown on the right and the top of the figure, respectively.

tions. This enlargement helped to decrease the fringing of the residual images in the next step, where we subtracted a median image from all frames. The median was created from a subset of frames that did not contain the target. We applied simple aperture photometry to the differential images based on the ephemeris (aperture central position in RA and Dec) provided by the *ephemd* tool (Pál et al. 2020). We then discarded data points that were contaminated by the residuals of the stellar images, saturation columns and crosstalk patterns from the camera electronics – the frequency of incidence of these data points is characterised by the duty cycle, the ratio of the number of frames used for the final light curve derivation and the total number of frames on which the target was theoretically visible. In the case of four targets, 2001 XP₂₅₄, 2013 AT₁₈₃, 2014 WS₅₁₀ and 2015 BC₅₁₉ the targets were observed in two campaigns, C16 and C18. For these targets we used the merged C16 and C18 data. The main characteristics of the observations are listed in Table 5 in the Appendix. The distribution of the length of the observations and the respective duty cycle values are shown in Fig. 1.

2.2. Period determination

The light curves obtained were analysed with a residual minimization algorithm (Pál et al. 2016; Molnár et al. 2018). In this method we fit the data with a function $A + B \cos(2\pi f \Delta t) + C \sin(2\pi f \Delta t)$, where f is the trial frequency, $\Delta t = T - t$, where T is the approximate center of the time series, and A , B , and C are parameters to be determined. We search for the minimum in the dispersion curves for each frequency. As demonstrated in Molnár et al. (2018) the best fit frequencies

obtained with this method are identical to the results of Lomb–Scargle periodogram or fast Fourier transform analyses, with a notably smaller general uncertainty in the residuals.

Nevertheless, our period determination was cross-checked with the Fourier spectra obtained with the *Period04* package (Lenz & Breger 2004), and we also used these spectra to obtain an amplitude upper limit in the case of period non-detections. We typically accepted the period with the strongest minimum in the residual spectrum. It has already been reported in previous K2 data analysis (see e.g. Marton et al. 2020) that there is increased noise towards lower frequencies, typically below $f \leq 1$ cycle/day (c/d). We observed the same phenomenon in our TNO data as well. To cope with this increased noise we calculated a local r.m.s. noise in the Fourier spectrum for each frequency using a running box with sigma clipping filtering to exclude the spectral peaks from the noise calculation. This r.m.s. noise, σ_f , is presented as a blue curve in the figures in Appendix C. Similar noise curves (σ_r) have been derived for the normalised residual spectra.

We evaluated the sensitivity of the Fourier method by testing it on two kinds of synthetic light curves, typically considered for asteroids and transneptunian objects: a rotating tri-axial ellipsoid with axes $a \geq b \geq c$, rotating around axis c , and a contact binary, with two spherical bodies of radius $r_1 \geq r_2$. As expected, the Fourier method is less sensitive to non-sinusoidal light curves as in these cases the spectral power, or equivalently the light curve amplitude is distributed over several peak frequencies, most prominently the harmonics of the primary frequency. We found a factor of ~ 2 decrease of Fourier sensitivity in the case of contact binary light curves, and a decrease of 1.2–1.5 in the case of triaxial ellipsoids compared with sinusoidal light curves with the same amplitude.

Considering this decreased Fourier sensitivity we accepted the peak in the residual spectrum if at the peak frequency the normalised residual (A_r) in the normalised residual spectrum $A_r \geq 5\sigma_r$ and the amplitude in the Fourier spectrum at the same frequency $A_f \geq 3\sigma_f$. A frequency is considered to be *tentative* if $A_r \geq 5\sigma_r$ and $2.5\sigma_f \leq A_f \leq 3\sigma_f$. We consider the frequency with the highest A_r/σ_r value as the *primary* light curve frequency of the target, if the requirements above are met. In some cases there were multiple frequencies with similarly high A_r/σ_r values found in the residual spectrum. We also list these *secondary* frequencies in Table 1.

We also investigated our light curves using a second-order Fourier method (Harris et al. 1989) to distinguish between single and double peak light curves, compar-

ing the amplitudes of the first and second harmonics, A_1 and A_2 , respectively. A single peak light curve was accepted when $A_1 \geq A_2$, and a double peak light curve was accepted when $A_1 < A_2$. In some cases it was difficult to decide between the first and second harmonics as the two amplitudes were close to each other. In these cases we listed both periods in Table 1, with the preferred one listed first and marked as ‘primary’ period. We used these preferred periods later in the subsequent analysis in this paper.

For targets with a detected light curve period we used the maximum difference between the data points of the folded and binned light curve, and the data in the individual bins to calculate the uncertainty in the amplitude, using standard error propagation. In those cases when no clear light curve period could have been identified we used the r.m.s. noise curves to characterise the detectable amplitudes – for each target a single value, σ_f^1 , obtained at $f = 1$ cycle day $^{-1}$, is used in general.

3. RESULTS

3.1. Absolute magnitudes

We determined the absolute magnitudes of the targets, transformed from the K2 observations to the USNO B1.0 R-band photometric system as described above, in the same way as in Marton et al. (2020). We did not correct for the light curve variations (which are discussed in Sect. 3.2) but we used simple averag-

ing of the observed brightness values when we calculated the phase angle uncorrected absolute magnitudes (m_{11}^R), after a correction for the heliocentric and observer distances. As the phase angle ranges of the observations were rather small, a phase angle correction could not be reliably obtained from these data to calculate the phase angle corrected absolute magnitudes (m_{110}^R). Therefore, we used a β_R linear phase coefficient from Ayala-Loera et al. (2018), when it was available for a specific target, and in all other cases we used $\beta_R = 0.176 \pm 0.132$ mag deg $^{-1}$, the mean of the β_R -s of TNOs. These m_{11}^R and m_{110}^R values are listed in Table 5.

3.2. Light curves and detectability

Table 1 contains the main frequencies identified for our targets. We were able to identify light curve frequencies for 37 targets (see Table 1), of which 10 are considered to be tentative. The residual spectrum and the light curve(s) folded with the main characteristic frequency/frequencies are presented in Appendix B. In the case of 29 targets no peaks in the residual and Fourier spectra met the criteria defined above. In these cases we used the σ_f^1 values to characterise the amplitude upper limits, as listed in Table 1. In Appendix C we present the unfolded light curves and the Fourier spectra of these targets.

Table 1. Main frequencies identified in the light curves of our targets. The columns are: (1) objects name (provisional designation); (2-3) frequency and uncertainty (day $^{-1}$); (4-5) period and uncertainty (h, redundant with frequency); (6-7) light curve amplitude and uncertainty (mag); upper limits are 1σ values based on the mean Fourier amplitude throughout the spectrum. Note that usually there is a notable (up to a factor of two) increase in r.m.s. amplitude towards low frequencies, typically below ~ 1 c/d; (8) Flag: P – primary period; S – secondary period; T – tentative ($2.5 < \sigma_f < 3$ in the Fourier spectrum and $\sigma > 5$ in the residual spectrum); W – uncertainties in frequency/period include the uncertainty due to nearby minimum in the residual spectrum; 1/2: single peak/double peak period. (9) comments and literature data; References: BS13 – Benecchi & Sheppard (2013b); K06 – Kern (2006); LL06 – Lacerda & Luu (2006a); P02 – Peixinho et al. (2002); SJ02 – Sheppard & Jewitt (2002); T10 – Thirouin et al. (2010); T12 – Thirouin et al. (2012); T14 – Thirouin et al. (2014); TS18 – Thirouin & Sheppard (2018a); TS19 – Thirouin & Sheppard (2019a);

| Name (1) | f (2) | δf (3) | P (4) | δP (5) | Δm (6) | $\delta(\Delta m)$ (7) | flag (8) | comments (9) |
|---------------------------------|----------------|-------------------|------------------|-------------------|-------------------|---------------------------|--------------|--|
| (26375) 1999 DE ₉ | 1.046 1.883 | 0.006 0.007 | 22.947 12.745 | 0.130 0.047 | 0.081 0.100 | 0.017 0.019 | P S | $\Delta m < 0.10$, P > 12 h (SJ02) |
| (35671) 1998 SN ₁₆₅ | 4.251 8.520 | 0.014 0.014 | 5.646 2.817 | 0.019 0.005 | 0.106 0.080 | 0.027 0.027 | P/SP S/DP | $\Delta m = 0.15_{-0.030}^{+0.022}$, P = 10.0 \pm 0.8 h (P02) $\Delta m = 0.16 \pm 0.01$, P = 8.84 h or 8.70 h (LL06) |
| (66652) Borasisi | 1.208 | 0.002 | 19.868 | 0.032 | 0.216 | 0.057 | P | P = 6.4 \pm 0.1 (K06) |
| (80806) 2000 CM ₁₀₅ | – | – | – | – | <0.045 | – | – | $\Delta m < 0.14$ (TS19) |
| (119878) 2002 CY ₂₂₄ | – | – | – | – | <0.194 | – | – | – |
| (126154) 2001 YH ₁₄₀ | 0.876 | 0.006 | 27.397 | 0.172 | 0.229 | 0.019 | P | $\Delta m = 0.13 \pm 0.05$, P = 13.2 h (T10) |

Table 1 continued

Table 1 (continued)

| Name | f | δf | P | δP | Δm | $\delta(\Delta m)$ | flag | comments |
|---------------------------------|-------|------------|---------|------------|------------|--------------------|------|---|
| (1) | (2) | (3) | (4) | (5) | (6) | (7) | (8) | (9) |
| | 1.751 | 0.005 | 13.705 | 0.039 | 0.095 | 0.019 | S | |
| (127871) 2003 FC ₁₂₈ | 0.867 | 0.006 | 27.674 | 0.194 | 0.161 | 0.039 | – | |
| (135182) 2001 QT ₃₂₂ | – | – | – | – | <0.067 | – | – | |
| (138537) 2000 OK ₆₇ | 0.710 | 0.038 | 33.803 | 1.809 | 0.155 | 0.042 | T/W | P>6h (TS19) |
| (145480) 2005 TB ₁₉₀ | – | – | – | – | <0.025 | – | – | $\Delta m = 0.12 \pm 0.01$, P = 12.68 h (T12) |
| (149348) 2002 VS ₁₃₀ | 2.778 | 0.023 | 8.639 | 0.072 | 0.217 | 0.060 | T | $\Delta m \approx 0.1$ (TS19) |
| (160147) 2001 KN ₇₆ | – | – | – | – | <0.043 | – | – | |
| (182934) 2002 GJ ₃₂ | – | – | – | – | <0.044 | – | – | |
| (307463) 2002 VU ₁₃₀ | – | – | – | – | <0.019 | – | – | |
| (307616) 2003 QW ₉₀ | 0.278 | 0.011 | 86.331 | 3.515 | 0.145 | 0.025 | P | |
| | 0.540 | 0.010 | 44.444 | 0.789 | 0.147 | 0.028 | S | |
| (308379) 2005 RS ₄₃ | – | – | – | – | <0.017 | – | – | |
| (312645) 2010 EP ₆₅ | 1.932 | 0.006 | 12.422 | 0.039 | 0.122 | 0.019 | P | $\Delta m = 0.17 \pm 0.03$, P _s = 7.48 h (BS13) |
| (385266) 2001 QB ₂₉₈ | – | – | – | – | <0.030 | – | – | |
| (385437) 2003 GH ₅₅ | 0.114 | 0.002 | 210.526 | 3.693 | 0.402 | 0.060 | P | |
| | 2.562 | 0.003 | 9.3683 | 0.01062 | 0.165 | 0.034 | S/T | |
| (408832) 2001 QJ ₂₉₈ | – | – | – | – | <0.038 | – | – | |
| (420356) Praamzius | 0.352 | 0.004 | 68.182 | 0.775 | 1.433 | 0.181 | P | |
| | 9.108 | 0.002 | 2.635 | 0.001 | 0.536 | 0.218 | S/T | |
| (469420) 2001 XP ₂₅₄ | 0.514 | 0.005 | 46.719 | 0.422 | 0.282 | 0.056 | P/T | |
| | 0.205 | 0.004 | 117.157 | 2.328 | 0.275 | 0.056 | S/T | |
| (469421) 2001 XD ₂₅₅ | – | – | – | – | <0.039 | – | – | |
| (469505) 2003 FE ₁₂₈ | 3.106 | 0.004 | 7.727 | 0.011 | 0.230 | 0.046 | P | $\Delta m = 0.50 \pm 0.14$, P = 5.85 \pm 0.15 h (K06) |
| | 0.582 | 0.005 | 41.203 | 0.360 | 0.292 | 0.047 | S/T | |
| (469704) 2005 EZ ₂₉₆ | 5.074 | 0.005 | 4.730 | 0.005 | 0.431 | 0.093 | P | |
| | 0.596 | 0.006 | 40.268 | 0.404 | 0.514 | 0.083 | S | |
| (470523) 2008 CS ₁₉₀ | – | – | – | – | <0.022 | – | – | |
| (471137) 2010 ET ₆₅ | 0.724 | 0.005 | 33.149 | 0.217 | 0.124 | 0.020 | P | $\Delta m = 0.13 \pm 0.02$, P _s = 3.94 h (BS13) |
| | 1.452 | 0.006 | 16.529 | 0.064 | 0.105 | 0.019 | S | |
| (471150) 2010 FC ₄₉ | – | – | – | – | <0.010 | – | – | |
| (471318) 2011 JF ₃₁ | 9.030 | 0.006 | 2.658 | 0.002 | 0.487 | 0.045 | P | |
| | 4.515 | 0.003 | 5.316 | 0.003 | 0.443 | 0.044 | S | |
| (472235) 2014 GE ₄₅ | 2.386 | 0.036 | 10.059 | 0.151 | 0.501 | 0.074 | T | |
| (508869) 2002 VT ₁₃₀ | – | – | – | – | <0.034 | – | – | $\Delta m \approx 0.21$ (T14) |
| (523658) 2012 DW ₉₈ | 0.790 | 0.005 | 30.380 | 0.184 | 0.241 | 0.051 | T | – |
| (523687) 2014 DF ₁₄₃ | – | – | – | – | <0.015 | – | – | – |
| (523692) 2014 EZ ₅₁ | 7.500 | 0.005 | 3.200 | 0.002 | 0.145 | 0.026 | – | – |
| (523698) 2014 GD ₅₄ | 0.542 | 0.007 | 44.280 | 0.563 | 0.262 | 0.050 | T | – |
| (523706) 2014 HF ₂₀₀ | 4.808 | 0.016 | 4.992 | 0.016 | 0.516 | 0.064 | – | – |
| (523769) 2014 WS ₅₁₀ | 0.960 | 0.004 | 25.009 | 0.100 | 0.374 | 0.060 | – | – |
| (525462) 2005 EO ₃₀₄ | 0.658 | 0.006 | 36.474 | 0.306 | 0.515 | 0.094 | – | – |
| (533207) 2014 DJ ₁₄₃ | – | – | – | – | <0.040 | – | – | – |
| (533562) 2014 JQ ₈₀ | 1.974 | 0.005 | 12.158 | 0.032 | 0.394 | 0.137 | P | $\Delta m = 0.76 \pm 0.04$, P = 12.16 h (TS18) |
| | 3.948 | 0.010 | 6.079 | 0.015 | 0.403 | 0.101 | S | |
| (533676) 2014 LS ₂₈ | – | – | – | – | <0.041 | – | – | $\Delta m = 0.35 \pm 0.03$, P = 5.52/11.04 h (TS19) |
| (535018) 2014 WA ₅₀₉ | – | – | – | – | <0.054 | – | – | – |
| (535023) 2014 WO ₅₀₉ | – | – | – | – | <0.017 | – | – | – |
| (535028) 2014 WA ₅₁₀ | – | – | – | – | <0.021 | – | – | – |
| (535030) 2014 WJ ₅₁₀ | 0.592 | 0.009 | 40.541 | 0.648 | 0.442 | 0.094 | T/SP | – |
| (535228) 2014 YE ₅₀ | 0.421 | 0.009 | 56.970 | 1.236 | 0.414 | 0.083 | T | – |
| (535231) 2014 YJ ₅₀ | – | – | – | – | <0.058 | – | – | – |

Table 1 continued

Table 1 (continued)

| Name | f | δf | P | δP | Δm | $\delta(\Delta m)$ | flag | comments |
|---------------------------------|--------|------------|--------|------------|------------|--------------------|------|-------------------------------|
| (1) | (2) | (3) | (4) | (5) | (6) | (7) | (8) | (9) |
| (542258) 2013 AP ₁₈₃ | 4.792 | 0.010 | 5.008 | 0.010 | 0.440 | 0.078 | T | – |
| 2001 HZ ₅₈ | 4.671 | 0.005 | 5.138 | 0.005 | 0.457 | 0.100 | – | – |
| 2001 QX ₂₉₇ | – | – | – | – | <0.073 | – | – | – |
| 2001 XU ₂₅₄ | 1.360 | 0.005 | 17.654 | 0.064 | 0.523 | 0.102 | – | – |
| | 0.680 | 0.003 | 35.294 | 0.128 | 0.681 | 0.099 | – | – |
| 2003 QA ₉₂ | – | – | – | – | <0.045 | – | – | – |
| 2003 YS ₁₇₉ | 1.244 | 0.035 | 19.293 | 0.542 | 1.278 | 0.197 | T | – |
| 2004 TF ₂₈₂ | – | – | – | – | <0.036 | – | – | – |
| 2004 TV ₃₅₇ | – | – | – | – | <0.041 | – | – | – |
| 2004 XR ₁₉₀ | – | – | – | – | <0.026 | – | – | – |
| 2009 YG ₁₉ | 6.328 | 0.048 | 3.793 | 0.029 | 0.360 | 0.045 | P | – |
| | 3.166 | 0.046 | 7.581 | 0.111 | 0.365 | 0.046 | S | – |
| 2013 AT ₁₈₃ | 0.305 | 0.002 | 78.788 | 0.346 | 0.402 | 0.051 | P | – |
| 2013 FA ₂₈ | – | – | – | – | <0.030 | – | – | $\Delta m \approx 0.1$ (TS19) |
| 2013 JV ₆₅ | 3.982 | 0.004 | 6.027 | 0.006 | 0.291 | 0.071 | – | – |
| 2014 AM ₅₅ | – | – | – | – | <0.032 | – | – | – |
| 2014 GJ ₅₄ | – | – | – | – | <0.047 | – | – | – |
| 2015 BB ₅₁₉ | 0.328 | 0.008 | 73.202 | 1.801 | 0.774 | 0.113 | – | – |
| 2015 BC ₅₁₉ | 2.697 | 0.005 | 8.899 | 0.006 | 0.330 | 0.061 | P | – |
| 2015 BZ ₅₁₈ | 0.760 | 0.004 | 31.579 | 0.083 | 0.392 | 0.079 | P | – |
| | 1.476 | 0.004 | 16.260 | 0.022 | 0.373 | 0.076 | S | – |
| 2015 DA ₂₂₅ | 6.7961 | 0.0034 | 3.531 | 0.002 | 0.511 | 0.128 | P | – |
| | 0.668 | 0.004 | 35.928 | 0.188 | 0.484 | 0.119 | S/T | – |

| Correlation | slope (mag/mag) | ρ_{Sp} | S_{Sp} | Fig. |
|-------------------------------------|--------------------|-------------|----------|------|
| Δm vs. \bar{m} , det. | 0.152±0.030 | 0.593 | 5.5e-5 | 2 |
| Δm vs. \bar{m} , non-det. | 0.053±0.001 | 0.728 | 7.54e-6 | 2 |
| Δm vs. H_V , K2+ | 0.072±0.022 | 0.433 | 0.005 | 3b |
| Δm vs. H_V , K2 | 0.068±0.032 | 0.354 | 0.032 | 3b |
| Δm vs. H_{min}^R , K2+ | 0.073±0.021 | 0.476 | 0.009 | 3c |
| Δm vs. H_{min}^R , K2 | 0.073±0.031 | 0.339 | 0.040 | 3c |

Table 2. Correlations between the light curve amplitude (Δm) and the mean apparent brightness (\bar{m}) or the H_V and H_{min}^R absolute magnitudes, listing the corresponding slope, the Spearman’s rank correlation coefficient ρ_{Sp} and the significance S_{Sp} . For the non-detections the 3σ upper limits are considered. K2 refers to the targets in this paper, K2+ includes Gonggong, 2007 JJ₄₃ and 2002 GV₃₁ in addition. The last column lists the numbers of the corresponding figures.

In Figure 2 we present the light curve amplitudes of our targets versus their mean brightness. Detectable amplitudes show the expected trend and only light curves with amplitudes $\Delta m \geq 0.5$ mag are detected at mean brightness values of $\langle m \rangle \gtrsim 23$ mag. Notably, no

large amplitude light curve was identified among the brighter targets at $\langle m \rangle \lesssim 21$ mag. Linear fits to the detected amplitudes and the upper limits versus the mean brightness of the targets are also shown in this figure, and the slopes and correlation coefficients are listed in Table 2. Both the detected light curve amplitudes and the upper limits show a fairly strong correlation with the mean brightness. We also fitted the upper limits (open circles) assuming a detection limit that is constant in flux density and independent of the brightness of the target, i.e. it is a higher fraction of the brightness for fainter targets (black dash-dotted curve). This provides a better fit than the linear correlation (dashed red line), with a $\sim 30\%$ lower total residual, and corresponds to a 3σ detection limit of $\Delta m = 0.0133$ mag at $\langle m \rangle = 20$ mag and $\Delta m = 0.21$ mag at $\langle m \rangle = 23$ mag mean brightness values.

We plot the amplitude of the light curves against the absolute magnitudes of our sample in Figure 3a; the detected light curve amplitudes versus H_V , separately (Figure 3b); and also the light curve amplitudes versus the corrected ‘Kepler band’ (i.e. USNO B1.0 R) absolute magnitude, $H_{min}^R = m_{110}^R - \Delta m/2$ (Figure 3c), as defined in Showalter et al. (2021). Targets with detected light curve period show a weak correlation between H_V or H_{min}^R and the light curve amplitude, at a similar

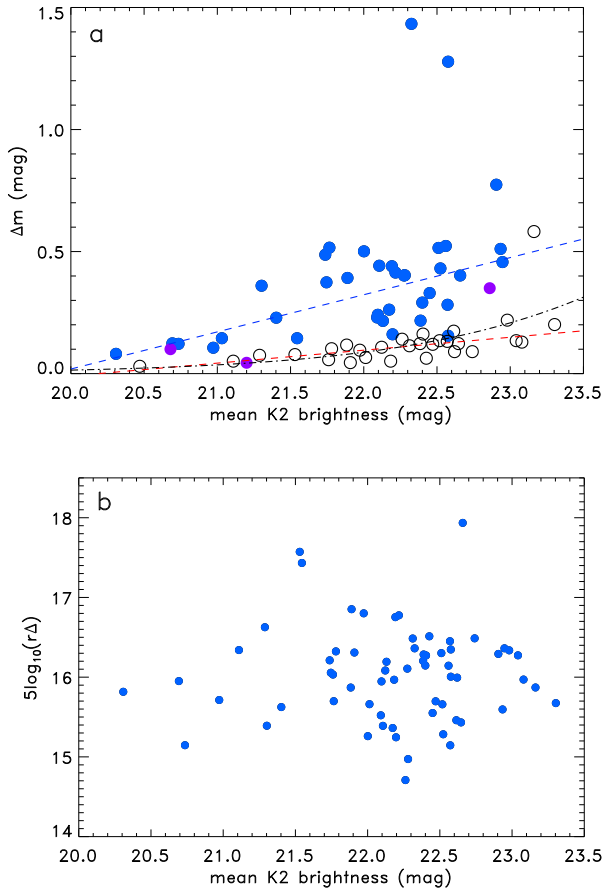


Figure 2. (a) Light curve amplitude as a function of mean brightness. Blue and black filled circles represent the K2 TNOs with detected periods, and those with a tentative frequency, respectively. The data of three previous K2 TNO light curve detections (purple symbols, Gonggong, 2007 JJ₄₃, 2002 GV₃₁, Pál et al. 2015, 2016) are also included. Open circles shows the TNOs without a detected period, in these cases the amplitude upper limit is obtained as $\Delta m = 3\sigma_f^1$. The blue and red dashed lines represent linear fits to the light curve amplitudes of the detections and the $3\sigma_f^1$ upper limits of period non-detections, respectively. The black dash-dotted curve corresponds to a constant flux density detection limit fitted to the non-detection upper limits, with $\Delta m = 0.0133$ mag at $\langle m \rangle = 20$ mag. (b) Distance modulus of our K2 targets versus their mean apparent brightness

level of significance as in Showalter et al. (2021), and with slopes similar to the Showalter et al. (2021) ‘non-OSSOS’ values, considering the large error bars on the slopes due to the weak correlations. The high slope values obtained for their OSSOS sample is not seen among our targets. While the correlation between H_V and Δm is often interpreted as a sign that smaller (higher H_V) objects could in general have higher light curve amplitudes (see e.g. Benecchi & Sheppard 2013a; Thirouin

& Sheppard 2019b) an apparent-brightness-dependent light curve amplitude detection limit – that we have seen above for our sample – may easily lead to a weak H_V – Δm correlation by selecting only the higher amplitude targets among the lowest- H_V ones, concealing their true behaviour. However, as demonstrated in Fig. 2b and 3d, we cannot observe notable correlation either between the apparent mean brightness and the distance modulus of the targets, nor between the absolute magnitude and the distance modulus which could explain a light curve amplitude – H_V correlation.

3.3. Individual objects (with previously “detected” light curve periods)

We have cross-checked our light curves with previous light curve detection of the same targets. While in some cases we can confirm the earlier light curve periods, in many cases our data clearly rules out the previous detection, as the usually high light curve amplitudes claimed in those papers should have clearly been detected in our data at those frequencies.

1999 DE₉—An upper limit of $\Delta m < 0.1$ mag was obtained on the light curve amplitude and a lower limit of $P > 12$ h on the period by Sheppard & Jewitt (2002); our new $P = 22.9$ h period and $\Delta m = 0.081$ mag amplitude are compatible with these previous values.

1998 SN₁₆₅—This target has two well-defined frequencies in the residual spectrum which are the first and second harmonics of the same frequency. Our analysis provided the double-peak period, $P = 5.646$ h being the more likely one. This period is different from the periods obtained by Peixinho et al. (2002) and Lacerda & Luu (2006a) ($P = 10.0$ h and 8.84 h or 8.70 h, respectively).

Borasisi—Kern (2006) obtained a rotation period of $P = 6.4 \pm 0.1$ h, using data from one single night to determine the light curve period, and another night with some spare phase coverage almost a year later, when the fixed period from the first date was used to phase the data. We could not recover this period from our data, but identified a single prominent period at $f = 1.208 \pm 0.002$ c/d or $P = 19.868 \pm 0.032$ h, with an amplitude of $\Delta m = 0.216 \pm 0.057$ mag.

2000 CM₁₀₅—A light curve amplitude estimate of $\Delta m \approx 0.14$ mag was obtained by Thirouin & Sheppard (2019a) which is about the 3σ limit of our data. We have not detected any period for this target though.

2001 YH₁₄₀—Our *single-peak* period, $P = 13.705$ h is roughly compatible with the 13.2 h period obtained by Thirouin et al. (2010), however, we identified the double period, $P = 27.397$ h as the more likely one.

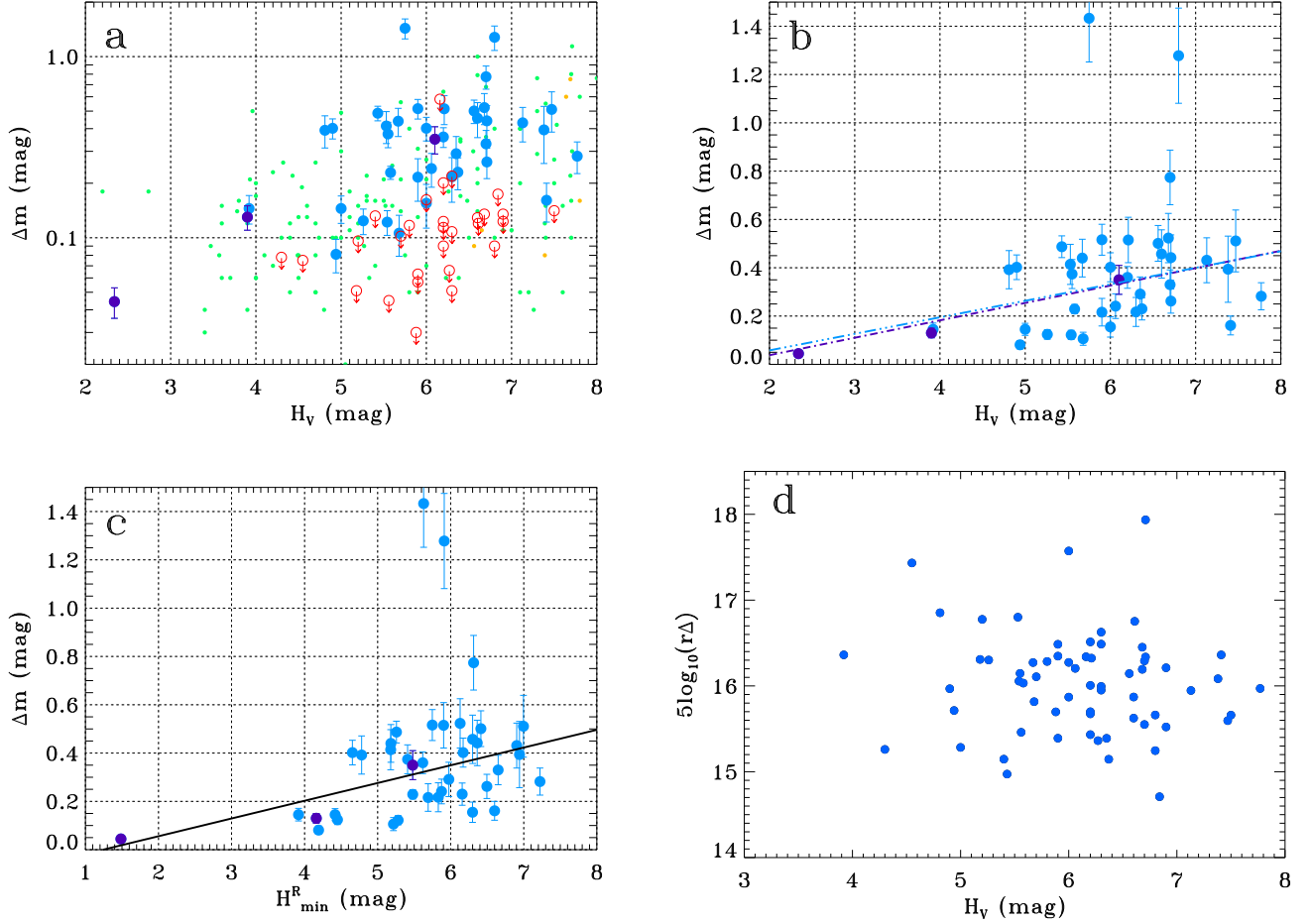


Figure 3. a) Light curve amplitude (Δm) versus the V-band absolute magnitude (H_V). Green and orange symbols are TNOs and Centaurs from the LCDB (using the maximum amplitude value); Blue symbols correspond to TNOs with detected periods from our K2 survey (this paper); Red symbols are amplitude upper limits of TNOs without detected periods from our K2 survey (this paper, represented by $3\sigma_f$ at $f=1$ c/d). Purple symbols are K2 measurements of Gonggong (2007 OR₁₀), 2002 GV₃₁, and 2007 JJ₄₃ (Pál et al. 2015, 2016). b) Δm versus H_V relationship of K2 TNOs with a linear fit. The purple dash-dotted and blue dash-triple-dotted lines correspond to fits with and without Gonggong, respectively. c) The same as b) but using $H_{min}^R = m_{110}^R - \Delta m/2$ instead of H_V . The linear fits to the data with and without Gonggong are so close to each other that they are represented by a single solid line. d) Distance modulus versus V-band absolute magnitude.

2005 TB₁₉₀—While a light curve with a period of $P = 12.68$ h and amplitude of $\Delta m = 0.12$ mag was identified by Thirouin et al. (2012) we could only obtain a 3σ amplitude upper limit of $\Delta m = 0.075$ mag for this target. We could not identify any peak in the spectrum at the corresponding frequency.

2010 EP₆₅—The $P = 7.48$ h period obtained by Benecchi & Sheppard (2013b) could not be recovered from our data. Instead, a very prominent period of $P = 12.422$ h with $\Delta m = 0.122$ mag was identified from our K2 measurements.

Praamzius—A prominent minimum was identified at the low-frequency part of the residual spectrum at $f = 0.352 \pm 0.004$ c/d, $P = 68.182 \pm 0.775$ h, with a large light curve amplitude of $\Delta m = 1.433 \pm 0.181$ mag. There is another, prominent minimum at the high-frequency part at $f = 9.108 \pm 0.002$ c/d ($P = 2.635 \pm 0.001$ h, $\Delta m = 0.536 \pm 0.218$ mag) that technically meets the criterion of a detection. However, we consider this frequency as tentative and use $f = 0.352 \pm 0.004$ c/d as the primary frequency.

2003 FE₁₂₈—While two rather different possible light curve periods were identified ($P = 7.727$ and 41.203 h)

from our K2 data, no notable peak could be found at the previously found $P = 5.85$ h period (Kern 2006).

2010 ET₆₅—Two prominent frequencies were obtained which correspond to the single/double peak light curves with the same base period ($P = 16.529$ and 33.149 h). We found no indication for the short period of $P = 3.94$ h found earlier by Benecchi & Sheppard (2013b).

2002 VT₁₃₀—A light curve amplitude estimate of $\Delta m \approx 0.21$ mag was obtained by Thirouin et al. (2014) which is notably higher than our $\Delta m = 0.1$ mag 3σ amplitude upper limit. Despite that we could not detect any light curve period for this target.

2014 JQ₈₀—A prominent contact binary signal was detected for 2014 JQ₈₀ by Thirouin & Sheppard (2018a) (TS18), with a double-peaked light curve period of $P = 12.16$ h. Our analysis provided the period $P = 6.079$ h, ($f = 3.948$ c/d) with the highest signal-to-noise over the r.m.s. noise in the residual spectrum. This is exactly the half of that found by Thirouin & Sheppard (2018a), and agrees their single-peak period. While our associated light curve amplitude is definitely smaller than the Thirouin & Sheppard (2018a) one, this is expected considering the faintness of the target and the relative accuracy that could be achieved in K2 measurements due to the small telescope size and long integration times relative to the rotation period and compared with the width/depth of the minima of a contact binary light curve. Finding the previously identified period of 2014 JQ₈₀ is a good example that our method can effectively select the 'right' periods from multiple possibilities.

2014 LS₂₈—(Thirouin & Sheppard 2019a) obtained a light curve period of $P = 5.52$ or 11.04 h, with a rather high amplitude of $\Delta m = 0.35$ mag. Although our 3σ amplitude upper limit of ~ 0.12 mag is significantly lower than this amplitude, we could not find these periods in our data.

2013 FA₂₈—A light curve amplitude estimate of $\Delta m \approx 0.1$ mag was obtained by Thirouin & Sheppard (2019a) which is close to our $\Delta m = 0.1$ mag 3σ amplitude upper limit. We could not detect any light curve period for this target.

3.4. Amplitude distribution

We compared our cumulative amplitude distribution with those discussed in Showalter et al. (2021). To obtain the cumulative amplitude distribution curve of our K2 sample we considered both the targets with detected periods and well-determined amplitudes, and also those which only have amplitude upper limits (see Fig. 4). The

amplitude upper limits in our sample were considered in three different ways when drawing the cumulative amplitude distributions: (1) using $\Delta m = 0$ for all non-detections (brown dashed curve in Fig. 4); (2) assigning a random amplitude value assuming an underlying normal distribution and using the 1σ detection limit as standard deviation around zero amplitude (black solid curve); and (3) using $\Delta m = 3\sigma$ for all non-detections (purple dash-dotted curve). The light curve amplitudes of the targets with detected periods were considered with their actual value as an expectation value, using the amplitude uncertainty as standard deviation. We generated a thousand curves in each case, and their median curve is considered as our K2 cumulative amplitude distribution, presented in Fig. 4. Cases (1) and (3) represent the two most extreme cases for the underlying amplitude distribution of our non-detections and due to the preference of small amplitudes in Case (2) the true cumulative amplitude curve is very likely between the curves of Cases (2) and (3). Above $\Delta m \approx 0.1$ mag there is no real difference between the curves of (1), (2) and (3).

In the same figure we also plot the 'Combined', 'Centaur' and 'OSSOS' curves from Showalter et al. (2021) which mostly use ground-based data. We also plot the original cumulative amplitude curve derived by the Thousand Asteroid Light Curve Survey (Masiero et al. 2009) to cover the main belt asteroids. There is a considerable difference between the ground-based and the K2 cumulative amplitude distribution curves of transneptunian objects: a notably larger number of objects appear at low amplitudes compared with any of the curves derived by Showalter et al. (2021). As mentioned in Showalter et al. (2021), there may be multiple bias factors in their KBO amplitude statistics, e.g., high light curve amplitude targets are more favourably detected and reported than low amplitude targets from ground based observations. This alone can explain the difference between any of their distribution curves and our K2 one; the consideration of non-detections naturally increases the cumulative probability at low amplitudes. While our K2 sample cannot be considered to be non-biased, it is from a sample in which targets were selected merely by their celestial location (to be in actual K2 fields), and no other criteria (brightness, dynamic class, etc.) were applied. As biases in the ground-based data dominated sample are hard to be corrected for, we believe that our K2 cumulative amplitude curve is currently the best representation of the KBO light curve amplitude distribution.

Showalter et al. (2021) compared their cumulative amplitude distributions to a group of models assuming sin-

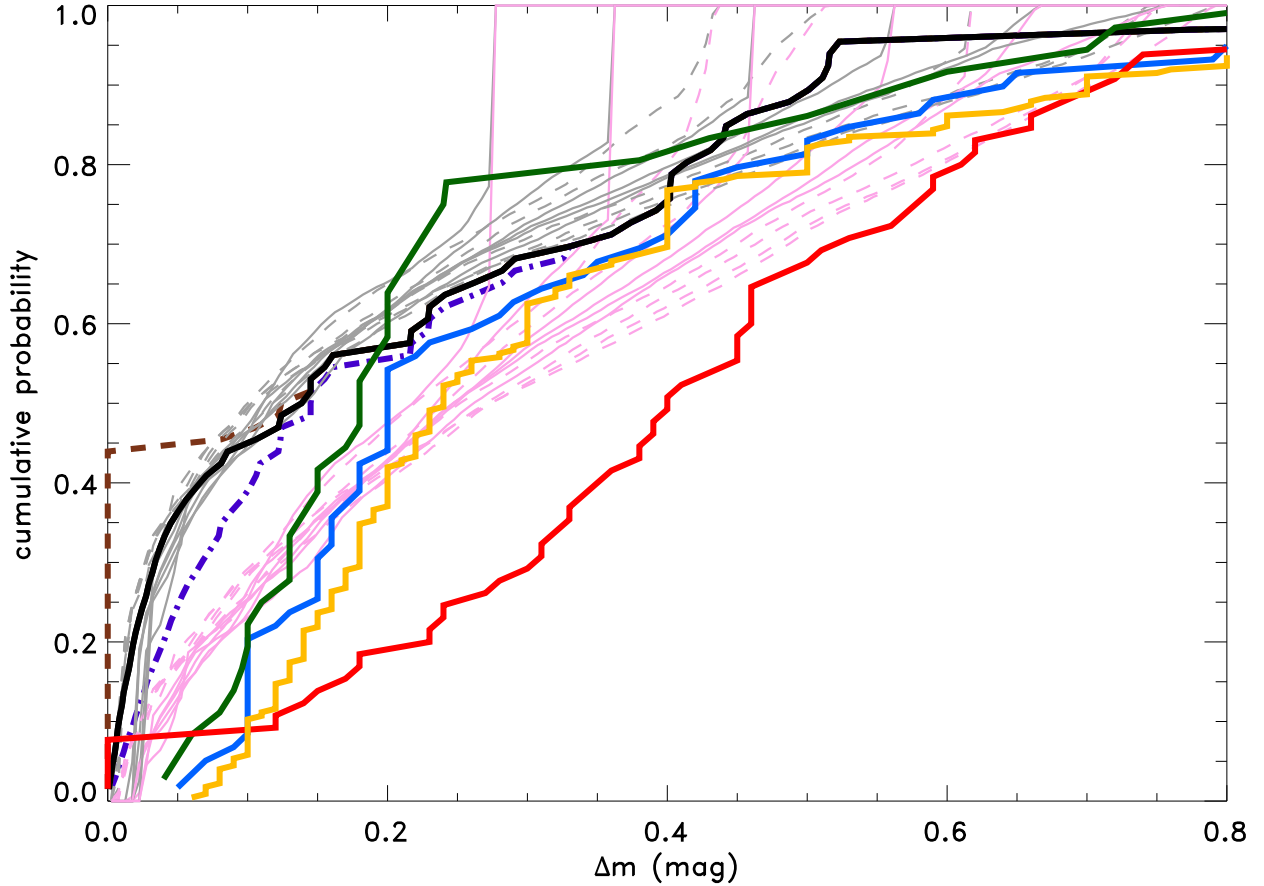


Figure 4. Cumulative amplitude distribution of the K2 TNOs. The brown (dashed), black (solid) and purple (dash-dotted) curves represent our TNO sample, assuming different distributions for the non-detections, as discussed in Sect. 3.4 (Cases (1), (2) and (3), respectively). The blue, green and red curves correspond to the ‘Combined’, ‘Centaur’ and ‘OSSOS’ curves in Fig. 11 in Showalter et al. (2021). The pale gray and pink curves in the background show the cumulative amplitude distribution of contact binaries assuming spherical shapes, size ratios from 0.5 to 1.0, Lambert (gray) or Lommel-Seeliger (pink) scattering, and either uniform aspect angle (solid curves) or isotropic pole orientation (dashed curves) distributions for a set of simulated objects (see a more detailed discussion in Showalter et al. (2021)). The yellow curve is the cumulative amplitude distribution in the main belt as derived in Masiero et al. (2009).

gle triaxial bodies or contact binaries with various configurations. As any specific curve could be fitted with a weighted combination of such curves from various shape and scattering models, we do not aim to try to find a ‘best model population’ for our K2 curve. However, it is obvious from the Showalter et al. (2021) models that the current shape of the K2 curve (with a ‘bulge’ at low amplitudes) is expected to be best fitted with ‘contact binary’-type curves. To demonstrate this we also calculated model cumulative amplitude curves of contact binaries assuming spherical shapes, size ratios from 0.5 to 1.0, Lambert or Lommel-Seeliger scattering, and either uniform aspect angle or isotropic pole orientation distributions for a set of simulated objects (pale gray and pink curves in Fig. 4). In this very simple approach the

best match is provided by models with Lambert scattering and uniform aspect angle distribution, but our relatively poor statistics does not allow for a more profound analysis of the underlying shape distribution, especially if light curve of binaries and elongated objects have to be combined.

Our K2 TNO cumulative amplitude curve is also different from the K2 Hilda and Jovian Trojan curves which have a notably lower number of objects at small amplitudes – in this sense the Hilda and Jovian Trojan curves are more similar to the main belt cumulative amplitude distribution (Masiero et al. 2009) where the light curve amplitude distribution is explained by elongated objects with a large fraction of asteroids with axis ratios $b/a \sim 0.8$, and a smaller distinct group at $b/a \sim 0.3$. A

$\sim 20\text{-}25\%$ binary fraction among Hildas and Jovian Trojans indicated by the K2 data (Ryan et al. 2017; Szabó et al. 2017, 2020; Kalup et al. 2021) would still mean that the majority of these light curve can be explained by elongated bodies.

3.5. Light curve period distribution

The light curve period distribution obtained from K2 mission data was found to be substantially different from that of ground based measurements, with a notably higher fraction of slowly rotating objects found in K2 measurements, throughout all Solar system small body populations (Szabó et al. 2017, 2020; Kalup et al. 2021; Molnár et al. 2018). The same difference was observed for main belt asteroids using about ten thousand light curve obtained from TESS data (Pál et al. 2020). Here we compare our period distribution (using our detected light curve frequencies/periods) with that obtained from the LCDB, and also with the K2 Hilda and Jovian Trojan distributions in Table 3 and Figs. 5 and 6.

As demonstrated in Table 3 and Fig. 5 K2 TNOs show a similar fraction of $\sim 38\%$ of slow rotators ($f \leq 0.8 \text{ d}^{-1}$, see Pravec & Harris 2000) than that found among K2 Jovian Trojans and Hildas, and this fraction is much higher than that in the LCDB TNO data ($\sim 3\%$). While the fraction of very slow rotators ($f \leq 0.24 \text{ d}^{-1}$) is relatively high among Jovian Trojans and Hildas (13 and 18%) these are essentially missing from the K2 TNO sample (2.5%). The median light curve frequency is $\sim 1.00 \text{ c/d}$ ($\sim 24.0 \text{ h}$) among the K2 TNOs while it is $\sim 2.7 \text{ c/d}$ ($\sim 8.9 \text{ h}$) among LCDB TNOs. This $\sim 1 \text{ d}$ K2 TNO median light curve period is even longer than those of K2 Jovian Trojans and Hildas. Note that while the absolute magnitude (and therefore the size) range we explore is similar or at least somewhat overlapping for Jovian Trojans and Hildas (see Fig. 6), it is very different for the K2, as well as the LCDB TNOs. It means that we are looking at objects about an order of magnitude larger among TNOs, in the $D \geq 100 \text{ km}$ diameter range. Some possible consequences are discussed in Sect. 4.

Thirouin & Sheppard (2019a) compared the mean light curve periods of cold classical TNOs and TNOs in other dynamical classes and found that cold classicals rotate somewhat slower (mean rotation periods of $\bar{P}(CC) = 9.47 \pm 1.53 \text{ h}$ and $\bar{P}(\text{non-CC}) = 8.45 \pm 0.58 \text{ h}$). These values are significantly different from our median rotation periods (20.00 h and 26.37 h), and in our sample cold classicals rotate slightly faster, however, the small difference between the two groups is likely due to statistical errors than real physical differences.

3.6. Light curve amplitude versus frequency

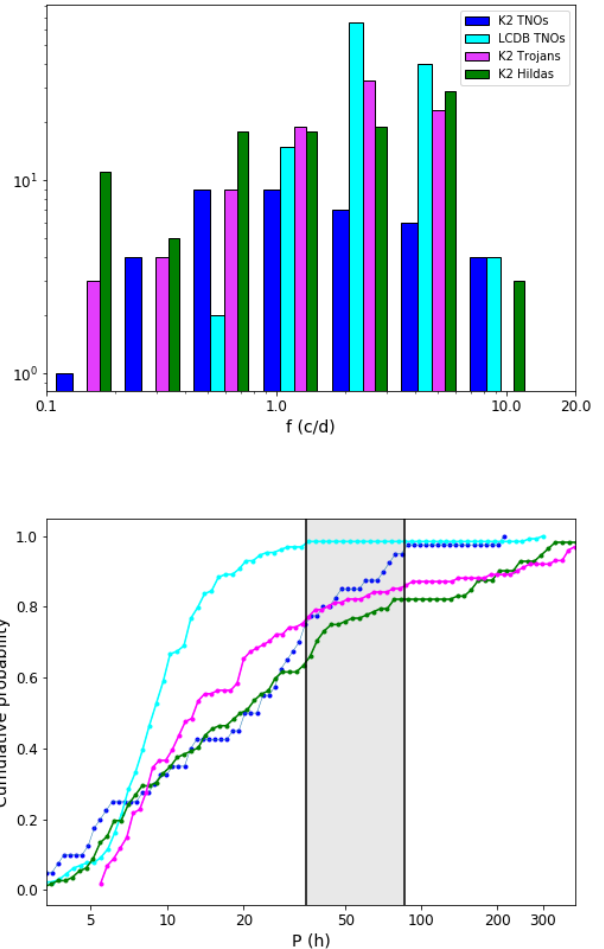


Figure 5. Top panel: Frequency distribution of asteroids. The cyan, magenta, green and blue colours represent the TNOs in the LCDB and Jovian trojans, Hildas and TNOs from K2, respectively. Bottom panel: Cumulative distribution of the same data sets as in the top panel. The gray regime between the vertical black lines shows where TNOs overcome Hilda asteroids.

The light curve amplitude versus rotational frequency plane (see Fig. 7) is usually divided into three main zones (Leone et al. 1984; Sheppard & Jewitt 2004; Thirouin et al. 2010; Benecchi & Sheppard 2013a). Light curve variations of objects with small amplitudes ($\Delta m \leq 0.25 \text{ mag}$ or 0.15 mag) can either be caused by albedo and shape features or can as well be binaries (colored areas in Fig. 7). If the rotational equilibrium of a strengthless body is considered and approximated by a Jacobi ellipsoid, constant density curves can be drawn (blue dash-dotted curves in Fig. 7) Lacerda & Jewitt (see eqs. 1 & 2 in 2007, and references therein), assuming $\vartheta = \pi/2$ aspect angle, i.e. equator-on viewing

| | TNOs LCDB | K2 TNOs full | K2 TNOs non-CC | K2 TNOs CC | K2 JTs | K2 Hildas |
|--------------|------------------------|------------------------|------------------------|------------------------|------------------------|------------------------|
| N | 129 | 40 | 30 | 10 | 101 | 112 |
| f_m (c/d) | $2.71^{+1.63}_{-0.34}$ | $1.00^{+2.10}_{-0.33}$ | $1.00^{+2.30}_{-0.28}$ | $1.01^{+1.53}_{-0.51}$ | $1.90^{+1.34}_{-0.79}$ | $1.22^{+1.88}_{-0.69}$ |
| H_V (mag) | 6.26 ± 2.66 | 5.90 ± 0.97 | 5.79 ± 1.12 | 6.25 ± 0.55 | 11.6 ± 0.99 | 13.7 ± 1.07 |
| P_m (h) | 8.85 | 23.94 | 24.00 | 23.76 | 12.63 | 19.67 |
| N_f | 3 | 2 | 2 | 0 | 0 | 2 |
| r_f (%) | 2.3 | 5.0 | 6.66 | 0 | 0 | 1.8 |
| N_s | 4 | 15 | 12 | 3 | 26 | 43 |
| r_s (%) | 3.1 | 37.5 | 40.0 | 30.0 | 25.7 | 38.9 |
| N_{vs} | 2 | 1 | 0 | 1 | 13 | 20 |
| r_{vs} (%) | 1.5 | 2.5 | 0 | 10.0 | 12.9 | 17.85 |

Table 3. Summary table containing some basic statistics, including the number of asteroids (N), median rotation rates (f_m) and the corresponding rotation period (P_m), and the fraction of targets in the fast, slow, and very slow rotator groups of the LCDB TNOs, K2 TNOs (this work), K2 Jovian trojans (Szabó et al. 2017; Kalup et al. 2021) and K2 Hildas (Szabó et al. 2020). Fast rotators (subscript ‘f’) are defined as $f \geq 7 \text{ d}^{-1}$, slow rotators (‘s’) as $f \leq 0.8 \text{ d}^{-1}$ and very slow rotators (‘vs’) as $f \leq 0.24 \text{ d}^{-1}$.

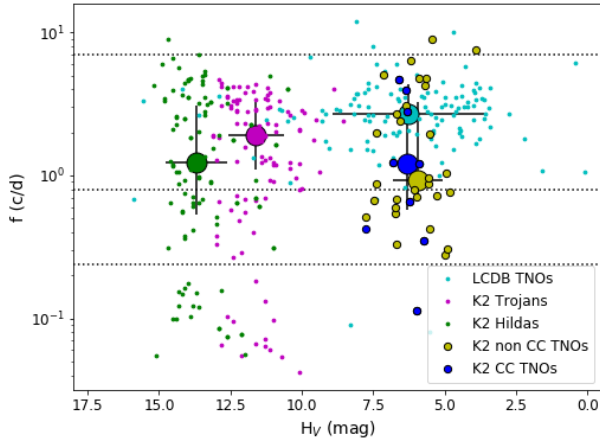


Figure 6. Frequency as a function of absolute magnitude. Big circles with error bars mark the median values with standard deviations for the different samples. The actual values are listed in Table 3. The boundary of fast, slow and very slow rotators are also added on the figure (black dotted lines).

geometry and maximum light curve amplitude. Objects to the right of a curve of a constant density are likely rotating single bodies, if their rotational speed is below the breakup limit Pravec & Harris (see 2000), and the left panel of Fig 7. Rotations of the objects to the left of a constant density Jacoby ellipsoid curve are too slow to cause elongation and their corresponding rotational light curve. For these objects the light curves are sometimes explained by binarity (see Marton et al. 2020, for a discussion).

The typical density of Kuiper belt objects in the size range of our study – 100–1000 km, see Table 5 – is 0.5–

1.0 g cm^{-3} (Grundy et al. 2019) and density estimates from binary orbits of Kuiper belt objects range from $\rho = 0.44^{+0.44}_{-0.17} \text{ g cm}^{-3}$ (Typhon-Echinda, Grundy et al. 2008) to $\rho = 1.37^{+0.66}_{-0.32} \text{ g cm}^{-3}$ (Ceto-Phorcys, Grundy et al. 2007). Smaller objects with sizes of a few kilometers may have similar or somewhat lower densities and high porosities. E.g. the density of Arrokoth was estimated to be 0.235 g cm^{-3} (Keane et al. 2022), while the bulk density of 67P is 0.533 g cm^{-3} (Pätzold et al. 2016).

Based on their location on the amplitude-frequency diagram the density of Hildas and Jovian Trojans were estimated to be $\lesssim 0.5 \text{ g cm}^{-3}$ using a $\sim 5 \text{ h}$ spin period limit (Ryan et al. 2017; Szabó et al. 2017, 2020; Kalup et al. 2021) for diameters $D \gtrsim 10 \text{ km}$. The study by Chang et al. (2021) included smaller objects down to $D \sim 2 \text{ km}$, and estimated a bulk density of 0.9 g cm^{-3} for Jovian Trojans, and Chang et al. (2022) obtained a bulk density of 1.5 g cm^{-3} for Hildas from the light curves of small objects of $1 \leq D \leq 3 \text{ km}$.

Majority of the TNOs both in our K2 sample and in the LCDB can be found at frequency-amplitudes characterised by low Jacobi ellipsoid and breakup limit densities, typically below $\rho = 0.5\text{-}1.0 \text{ g cm}^{-3}$. There are a few objects in our K2 sample, however, which have relatively high spin frequencies (e.g. 2011 JF₃₁, 2005 EZ₂₉₆ and 2009 YG₁₉, see Table 4 and Fig. 9). These targets would require high, $\rho \geq 2.0 \text{ g cm}^{-3}$ density and/or considerable internal strength to maintain their rotational state with rotation periods $\sim 3 \text{ h}$, or faster. For most of these targets a single peak light curve is associated with the primary frequency. Despite that our analysis found these light curve frequencies to be the most likely ones, a double peak light curve, and a corresponding double period is similarly likely which would also reduce the

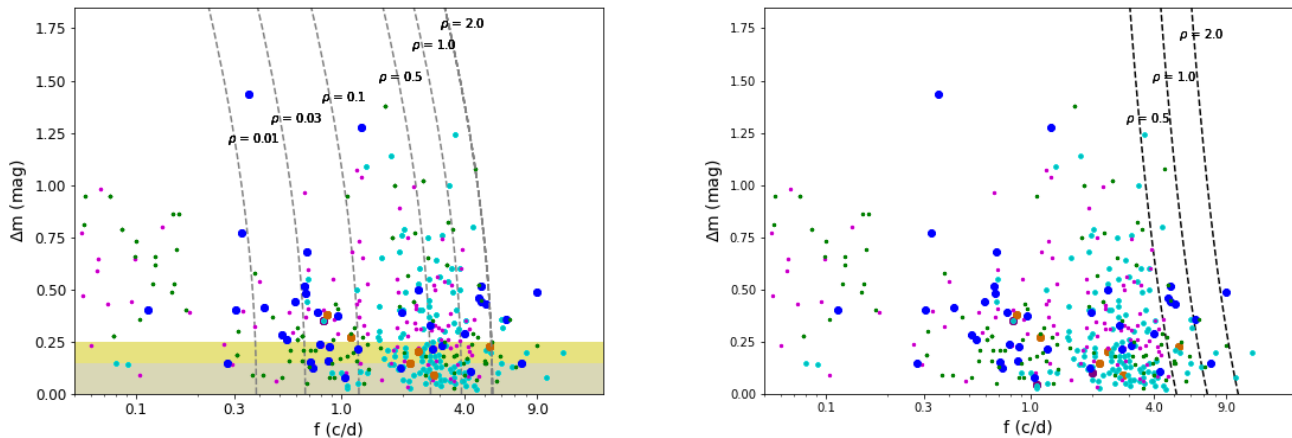


Figure 7. Left panel: Light curve amplitude as a function of the light curve (rotational) frequency. Colour coding is the same as in the previous figures; brown filled circles show the Centaurs from Marton et al. (2020). Each dashed curve represent a specific density (indicated by the numbers in units of $g \cdot cm^{-3}$) that corresponds to the rotation of a strengthless body with the shape of a Jacobi ellipsoid. Right panel: Here the same data are presented as on the left panel, but instead of the constant density Jacobi ellipsoid curves here we show the critical density curves calculated as $\Delta m = (\rho_c / [1 g cm^{-3}]) (f / [7.27 c/d])^{-2} - 1$ (Pravec & Harris 2000).

density/internal strength limits for these objects. However, even in this case the rotation periods are shorter than the fastest ones in the Jovian Trojan K2 sample. This suggests that moderate density objects ($\rho = 1.0$ - $2.0 g cm^{-3}$) may exist in the transneptunian region at this few hundred kilometer size range, as previously obtained from the studies of binaries.

As in the previous cases of Jovian Trojans, Hildas and Centaurs observed by K2 (Szabó et al. 2017, 2020; Marton et al. 2020; Kalup et al. 2021) a considerable fraction of our targets falls into the low frequency - high amplitude regime where their rotation is traditionally explained by binarity. Simply considering the $\rho = 0.5 g cm^{-3}$ Jacobi ellipsoid curve and an amplitude limit of $\Delta m = 0.25 mag$ 21% of the K2 targets would fall into the 'binary' category which is very similar to the values obtained in the K2 samples of other populations (Ryan et al. 2017; Szabó et al. 2017, 2020; Marton et al. 2020; Kalup et al. 2021).

4. CONCLUSIONS

Little is known about the true shape of transneptunian objects. Accurate shapes are available for those visited by a spacecraft, and at the large end of the size range Pluto and Charon were found to be very round (Nimmo et al. 2017). On the small end of the size range, however, Arrokoth was most probably formed by a merger of two bodies, and has a bilobate shape (see e.g. Keane et al. 2022). In recent years combination of light curve and oc-

cultation measurements have revealed the shape and size of some Centaurs and transneptunian objects, including 2002 GZ32 (Santos-Sanz et al. 2021), 2003 AZ₈₄ (Dias-Oliveira et al. 2017), Huya (Santos-Sanz et al. 2022), Chariklo (Morgado et al. 2021), 2002 VS₂ (Vara-Lubiano et al. 2022) and Haumea (Ortiz et al. 2017). While the very distorted shape of Haumea is certainly caused by its fast rotation, the other targets also show triaxial ellipsoid shapes as discussed in the respective papers. These objects are either small, below $D \approx 300 km$, or moderately deformed at larger sizes.

Our work samples the largest asteroids in the transneptunian region (in most cases $D \geq 200 km$, see Table 5) which are, as discussed above, believed to be primordial with their rotational characteristics have likely not been considerably modified since their formation, assuming that they are single bodies. It is generally accepted that periodic changes in asteroid light curves are caused by asteroid rotation due to either deformed shape or albedo variegations on the surface of a spherical (or rotationally flattened) body (see e.g. Lacerda & Luu 2003). In the last decades most works have tried to explain the light curves by deformed shape, and light curve inversion techniques have been very successful in this matter (see e.g. Durech et al. 2015).

The vast majority of the main belt asteroids studied this way have diameters $D \leq 100 km$ and therefore their shapes are not expected to be close that of hydrostatic equilibrium, due to their insufficient mass and gravity.

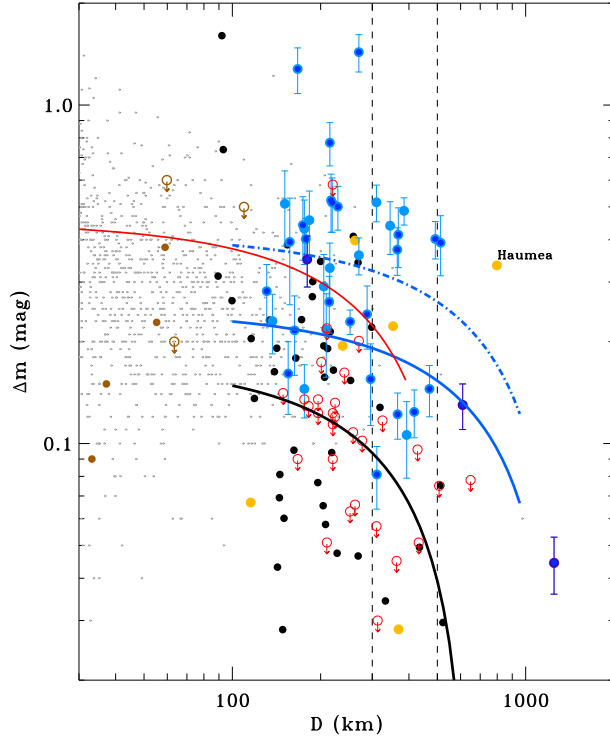


Figure 8. Light curve amplitude versus the estimated size of the targets in our sample. Symbols/colors are the same as in Fig. 3; blue symbols with dark blue ‘cores’ mark those targets for which the actual rotation period would indicate a density $\rho \leq 0.5 \text{ g cm}^{-3}$ assuming a Jacobi ellipsoid. The region between the vertical dashed lines mark the irregular-to-spherical transition size range in the main belt. Black symbols represent the ‘deformed shape’ light curve amplitudes of main belt asteroids studied by Vernazza et al. (2021), and the solid black curve is the ‘mean’ light curve amplitude curve obtained from this sample (see the main text for a detailed explanation). The blue curves are the mean K2 TNO amplitudes considering the detections only (dash-dotted) and also considering non-detections (solid curve). Orange symbols correspond to the Centaurs and TNOs whose shape and size are obtained from the combination of occultation and light curve measurements; the dwarf planet Haumea is marked. Brown symbols represent the Centaurs from Marton et al. (2020). The solid red curve is the mean amplitude curve from Showalter et al. (2021).

Recent works using high resolution imaging (e.g. the VLT/SPHERE instrument Hanuš et al. 2020; Vernazza et al. 2020, 2021) show that asphericity drops sharply ($1 - \varphi \leq 0.01$) for objects $D \geq 400 \text{ km}$ in the main belt and the transitional size from ‘irregular’ to ‘spherical’ objects may be as low as $D \approx 300 \text{ km}$. This transitional size is expected to be even lower for the icy objects in the transneptunian region due to their lower com-

pressive strength (Lineweaver & Norman 2010). Notably TNOs in the $D \approx 500 \text{ km}$ size range have densities $\rho \leq 1 \text{ g cm}^{-3}$ and a considerable level of porosity (e.g. Bierson & Nimmo 2019; Grundy et al. 2019). Due to their lower densities TNOs are more susceptible to be deformed due to rotation, but as discussed above, most of the K2 TNO targets have spin rates too low to be deformed by rotation with any plausible bulk density. We note that the targets discussed in this paper have diameters $D < 1000 \text{ km}$ with the exception of Gonggong. These TNOs have low densities and high porosities, also suggesting that these smaller objects may have formed later, several million years after the time of CAI formation. Due to the insufficient heat from radiogenic decay they likely did not have enough heat to reach even partial differentiation, and may remain undifferentiated for their whole existence (Bierson & Nimmo 2019).

In this sense it is interesting to plot the light curve amplitudes of our targets versus their estimated size (Fig. 8). While there are only three objects with $D \geq 500 \text{ km}$ in our sample, there are a number of objects – both with and without detected light curve periods – that fall in the $300 \leq D \leq 500 \text{ km}$ transitional zone where asphericity – hence light curve amplitude – is expected to drop assuming a single rotating body and main belt composition. Main belt asteroids are already almost extinct in this size range, and so are Centaurs – for these bodies irregular shapes are expected in most cases. The light curve amplitudes of large main belt asteroids presented in Fig. 8 are not their actual light curve amplitudes, but they are derived from the Vernazza et al. (2021) triaxial ellipsoid shape models, calculated from the ratios of the semi-axes b/a and assuming homogeneous albedo distribution on the surface. The mean main belt curve is obtained assuming random spin axis orientations. Similar mean curves are derived from the K2 TNO data (blue curves in Fig. 8), considering the detections only, and including the non-detections by considering the upper limits assigning random and amplitudes to each non-detection from a normal distribution with a standard deviation corresponding to the 1σ upper limit around zero amplitude.

While the general trend is the same among K2 TNOs as among large main belt asteroids, the deformed shape light curve amplitude is notably, a factor of 2-3 higher among TNOs than in the main belt, in contrast to the expectation. This remains true even if the lower TNO densities are considered: the majority of the K2 TNO targets would require very low ($\rho \ll 0.5 \text{ g cm}^{-3}$) densities to be deformed by rotation with their actual low spin rate. (Showalter et al. 2021) found a similar trend (see the red curve in Fig. 8), however, the sam-

ple they consider in their paper is restricted to targets with $H_V \gtrsim 5.5$ mag ($D \lesssim 400$ km) and cannot be readily extrapolated to larger sizes.

The contradiction of large amplitudes at large sizes compared with the main belt could be resolved if TNOs had higher-than-expected compressive strength and become spherical for sizes larger than their main belt counterparts, and remain 'irregular' in the $300 \leq D \leq 500$ km range. However, their general low density and high porosity point against this scenario. A notable fraction of contact or semi-contact binary systems in which the members themselves are in hydrostatical equilibrium could produce a population of high-amplitude light curves in this size range (Lacerda & Luu 2006b; Lacerda et al. 2014). As some authors have pointed out, contact binaries may be very frequent, especially in the plutino population (Thirouin & Sheppard 2018b, 2019b). However, a binary fraction higher than the currently deduced $\sim 20\%$ would be needed to explain the large number of large amplitudes among TNOs. The long term stability of such systems against their tidal evolution should also be investigated to answer the reliability of this assumption. Spherical (rotationally flattened spheroidal) bodies with large albedo variegations could also explain the observed large amplitudes. The large number of such objects would be a major difference compared to the main belt where most asteroids have relatively homogeneous albedo distributions on their surface.

The research leading to these results has received funding from the K-115709, K-138962, PD-116175, KKP-137523 and GINOP-2.3.2-15-2016-00003 grants of the National Research, Development and Innovation Office (NKFIH, Hungary); and from the LP2012-31 and LP2018-7/2021 Lendület grants of the Hungarian Academy of Sciences. The research leading to these results have been supported by the ÚNKP-19-2, ÚNKP-20-2 and ÚNKP-21-2 New National Excellence Programs of the Ministry of Innovation and Technology from the source of the National Research, Development and Innovation Fund. Funding for the *Kepler* and K2 missions are provided by the NASA Science Mission Directorate. The data presented in this paper were obtained from the Mikulski Archive for Space Telescopes (MAST). STScI is operated by the Association of Universities for Research in Astronomy, Inc., under NASA contract NAS5-26555. Support for MAST for non-HST data is provided by the NASA Office of Space Science via grant NNX09AF08G and by other grants and contracts. This research has made use of data and services provided by the International Astronomical Union's Minor Planet Center. The authors thank the hospitality of the Veszprém Regional Centre of the Hungarian Academy of Sciences (MTA VEAB), where part of this project was carried out. We are also thankful to our reviewers for their fair and balanced reports.

Facilities: Kepler/K2 (Howell et al. 2014)

Software: astropy (Astropy Collaboration et al. 2013, 2018), Period04 (Lenz & Breger 2004), fitsh (Pál 2012)

ACKNOWLEDGEMENT

REFERENCES

- Astropy Collaboration, Robitaille, T. P., Tollerud, E. J., et al. 2013, *A&A*, 558, A33, doi: [10.1051/0004-6361/201322068](https://doi.org/10.1051/0004-6361/201322068)
- Astropy Collaboration, Price-Whelan, A. M., Sipőcz, B. M., et al. 2018, *AJ*, 156, 123, doi: [10.3847/1538-3881/aabc4f](https://doi.org/10.3847/1538-3881/aabc4f)
- Ayala-Loera, C., Alvarez-Candal, A., Ortiz, J. L., et al. 2018, *MNRAS*, 481, 1848, doi: [10.1093/mnras/sty2363](https://doi.org/10.1093/mnras/sty2363)
- Benecchi, S. D., & Sheppard, S. S. 2013a, *AJ*, 145, 124, doi: [10.1088/0004-6256/145/5/124](https://doi.org/10.1088/0004-6256/145/5/124)
- . 2013b, *AJ*, 145, 124, doi: [10.1088/0004-6256/145/5/124](https://doi.org/10.1088/0004-6256/145/5/124)
- Bierson, C. J., & Nimmo, F. 2019, *Icarus*, 326, 10, doi: [10.1016/j.icarus.2019.01.027](https://doi.org/10.1016/j.icarus.2019.01.027)
- Chang, C.-K., Chen, Y.-T., Fraser, W. C., et al. 2021, *PSJ*, 2, 191, doi: [10.3847/PSJ/ac13a4](https://doi.org/10.3847/PSJ/ac13a4)
- . 2022, *ApJS*, 259, 7, doi: [10.3847/1538-4365/ac50ac](https://doi.org/10.3847/1538-4365/ac50ac)
- Dias-Oliveira, A., Sicardy, B., Ortiz, J. L., et al. 2017, *AJ*, 154, 22, doi: [10.3847/1538-3881/aa74e9](https://doi.org/10.3847/1538-3881/aa74e9)
- Duffard, R., Ortiz, J. L., Thirouin, A., Santos-Sanz, P., & Morales, N. 2009, *A&A*, 505, 1283, doi: [10.1051/0004-6361/200912601](https://doi.org/10.1051/0004-6361/200912601)
- Durech, J., Carry, B., Delbo, M., Kaasalainen, M., & Viikinkoski, M. 2015, *Asteroid Models from Multiple Data Sources* (University of Arizona Press, Tucson), 183–202, doi: [10.2458/azu_uapress.9780816532131-ch010](https://doi.org/10.2458/azu_uapress.9780816532131-ch010)
- Erasmus, N., Kramer, D., McNeill, A., et al. 2021, *MNRAS*, 506, 3872, doi: [10.1093/mnras/stab1888](https://doi.org/10.1093/mnras/stab1888)
- Farkas-Takács, A., Kiss, C., Pál, A., et al. 2017, *AJ*, 154, 119, doi: [10.3847/1538-3881/aa8365](https://doi.org/10.3847/1538-3881/aa8365)
- Farkas-Takács, A., Kiss, C., Vilenius, E., et al. 2020, *A&A*, 638, A23, doi: [10.1051/0004-6361/201936183](https://doi.org/10.1051/0004-6361/201936183)
- Giorgini, J. D., Yeomans, D. K., Chamberlin, A. B., et al. 1996, in *AAS/Division for Planetary Sciences Meeting Abstracts*, Vol. 28, AAS/Division for Planetary Sciences Meeting Abstracts #28, 25.04
- Gladman, B., Marsden, B. G., & Vanlaerhoven, C. 2008, in *The Solar System Beyond Neptune*, ed. M. A. Barucci, H. Boehnhardt, D. P. Cruikshank, A. Morbidelli, & R. Dotson (University of Arizona Press, Tucson), 43
- Grundy, W. M., Noll, K. S., Buie, M. W., et al. 2019, *Icarus*, 334, 30, doi: [10.1016/j.icarus.2018.12.037](https://doi.org/10.1016/j.icarus.2018.12.037)
- Grundy, W. M., Stansberry, J. A., Noll, K. S., et al. 2007, *Icarus*, 191, 286, doi: [10.1016/j.icarus.2007.04.004](https://doi.org/10.1016/j.icarus.2007.04.004)
- Grundy, W. M., Noll, K. S., Virtanen, J., et al. 2008, *Icarus*, 197, 260, doi: [10.1016/j.icarus.2008.04.004](https://doi.org/10.1016/j.icarus.2008.04.004)
- Hanuš, J., Pejcha, O., Shappee, B. J., et al. 2021, *A&A*, 654, A48, doi: [10.1051/0004-6361/202140759](https://doi.org/10.1051/0004-6361/202140759)
- Hanuš, J., Vernazza, P., Viikinkoski, M., et al. 2020, *A&A*, 633, A65, doi: [10.1051/0004-6361/201936639](https://doi.org/10.1051/0004-6361/201936639)
- Harris, A. W., Young, J. W., Bowell, E., et al. 1989, *Icarus*, 77, 171, doi: [10.1016/0019-1035\(89\)90015-8](https://doi.org/10.1016/0019-1035(89)90015-8)
- Howell, S. B., Sobek, C., Haas, M., et al. 2014, *PASP*, 126, 398, doi: [10.1086/676406](https://doi.org/10.1086/676406)
- Kalup, C. E., Molnár, L., Kiss, C., et al. 2021, *ApJS*, 254, 7, doi: [10.3847/1538-4365/abe76a](https://doi.org/10.3847/1538-4365/abe76a)
- Keane, J. T., Porter, S. B., Beyer, R. A., et al. 2022, *Journal of Geophysical Research (Planets)*, 127, e07068, doi: [10.1029/2021JE007068](https://doi.org/10.1029/2021JE007068)
- Kern, S. D. 2006, PhD thesis, Massachusetts Institute of Technology
- Kiss, C., Molnár, L., Pál, A., & Howell, S. 2020, *The Solar System as Observed by K2*, in *The NASA Kepler Mission*, ed. Howell, S.B. (IOP), 201–224
- Kiss, C., Pál, A., Farkas-Takács, A. I., et al. 2016, *MNRAS*, 457, 2908, doi: [10.1093/mnras/stw081](https://doi.org/10.1093/mnras/stw081)
- Lacerda, P., & Jewitt, D. C. 2007, *AJ*, 133, 1393, doi: [10.1086/511772](https://doi.org/10.1086/511772)
- Lacerda, P., & Luu, J. 2003, *Icarus*, 161, 174, doi: [10.1016/S0019-1035\(02\)00019-2](https://doi.org/10.1016/S0019-1035(02)00019-2)
- . 2006a, *AJ*, 131, 2314, doi: [10.1086/501047](https://doi.org/10.1086/501047)
- . 2006b, *AJ*, 131, 2314, doi: [10.1086/501047](https://doi.org/10.1086/501047)
- Lacerda, P., Fornasier, S., Lellouch, E., et al. 2014, *ApJL*, 793, L2, doi: [10.1088/2041-8205/793/1/L2](https://doi.org/10.1088/2041-8205/793/1/L2)
- Lellouch, E., Santos-Sanz, P., Lacerda, P., et al. 2013, *A&A*, 557, A60, doi: [10.1051/0004-6361/201322047](https://doi.org/10.1051/0004-6361/201322047)
- Lenz, P., & Breger, M. 2004, in *The A-Star Puzzle*, ed. J. Zverko, J. Ziznovsky, S. J. Adelman, & W. W. Weiss, Vol. 224, 786–790, doi: [10.1017/S1743921305009750](https://doi.org/10.1017/S1743921305009750)
- Leone, G., Paolicchi, P., Farinella, P., & Zappala, V. 1984, *A&A*, 140, 265
- Lineweaver, C. H., & Norman, M. 2010, arXiv e-prints, arXiv:1004.1091. <https://arxiv.org/abs/1004.1091>
- Marciniak, A., Pilcher, F., Oszkiewicz, D., et al. 2015, *Planet. Space Sci.*, 118, 256, doi: [10.1016/j.pss.2015.06.002](https://doi.org/10.1016/j.pss.2015.06.002)
- Marciniak, A., Bartczak, P., Müller, T., et al. 2018, *A&A*, 610, A7, doi: [10.1051/0004-6361/201731479](https://doi.org/10.1051/0004-6361/201731479)
- Marton, G., Kiss, C., Molnár, L., et al. 2020, *Icarus*, 345, 113721, doi: [10.1016/j.icarus.2020.113721](https://doi.org/10.1016/j.icarus.2020.113721)
- Masiero, J., Jedicke, R., Durech, J., et al. 2009, *Icarus*, 204, 145, doi: [10.1016/j.icarus.2009.06.012](https://doi.org/10.1016/j.icarus.2009.06.012)
- Molnár, L., Pál, A., Sárneczky, K., et al. 2018, *ApJS*, 234, 37, doi: [10.3847/1538-4365/aaa1a1](https://doi.org/10.3847/1538-4365/aaa1a1)
- Morgado, B. E., Sicardy, B., Braga-Ribas, F., et al. 2021, *A&A*, 652, A141, doi: [10.1051/0004-6361/202141543](https://doi.org/10.1051/0004-6361/202141543)
- Nesvorný, D., Vokrouhlický, D., Bottke, W. F., Levison, H. F., & Grundy, W. M. 2020, *ApJL*, 893, L16, doi: [10.3847/2041-8213/ab8311](https://doi.org/10.3847/2041-8213/ab8311)

- Nimmo, F., Umurhan, O., Lisse, C. M., et al. 2017, *Icarus*, 287, 12, doi: [10.1016/j.icarus.2016.06.027](https://doi.org/10.1016/j.icarus.2016.06.027)
- Noll, K., Grundy, W. M., Nesvorný, D., & Thirouin, A. 2020, *Trans-Neptunian binaries (2018)* (Elsevier), 201–224, doi: [10.1016/B978-0-12-816490-7.00009-6](https://doi.org/10.1016/B978-0-12-816490-7.00009-6)
- Ortiz, J. L., Santos-Sanz, P., Sicardy, B., et al. 2017, *Nature*, 550, 219, doi: [10.1038/nature24051](https://doi.org/10.1038/nature24051)
- Pál, A. 2012, *MNRAS*, 421, 1825, doi: [10.1111/j.1365-2966.2011.19813.x](https://doi.org/10.1111/j.1365-2966.2011.19813.x)
- Pál, A., Kiss, C., Müller, T. G., et al. 2016, *AJ*, 151, 117, doi: [10.3847/0004-6256/151/5/117](https://doi.org/10.3847/0004-6256/151/5/117)
- Pál, A., Szabó, R., Szabó, G. M., et al. 2015, *ApJL*, 804, L45, doi: [10.1088/2041-8205/804/2/L45](https://doi.org/10.1088/2041-8205/804/2/L45)
- Pál, A., Szakáts, R., Kiss, C., et al. 2020, *ApJS*, 247, 26, doi: [10.3847/1538-4365/ab64f0](https://doi.org/10.3847/1538-4365/ab64f0)
- Pätzold, M., Andert, T., Hahn, M., et al. 2016, *Nature*, 530, 63, doi: [10.1038/nature16535](https://doi.org/10.1038/nature16535)
- Peixinho, N., Doressoundiram, A., & Romon-Martin, J. 2002, *NewA*, 7, 359, doi: [10.1016/S1384-1076\(02\)00155-0](https://doi.org/10.1016/S1384-1076(02)00155-0)
- Pravec, P., & Harris, A. W. 2000, *Icarus*, 148, 12, doi: [10.1006/icar.2000.6482](https://doi.org/10.1006/icar.2000.6482)
- Pravec, P., Harris, A. W., & Michalowski, T. 2002, *Asteroid Rotations* (University of Arizona Press, Tucson), 113–122
- Ryan, E. L., Sharkey, B. N. L., & Woodward, C. E. 2017, *AJ*, 153, 116, doi: [10.3847/1538-3881/153/3/116](https://doi.org/10.3847/1538-3881/153/3/116)
- Santos-Sanz, P., Ortiz, J. L., Sicardy, B., et al. 2021, *MNRAS*, 501, 6062, doi: [10.1093/mnras/staa3881](https://doi.org/10.1093/mnras/staa3881)
- . 2022, arXiv e-prints, arXiv:2205.12882. <https://arxiv.org/abs/2205.12882>
- Sheppard, S. S., & Jewitt, D. 2004, *AJ*, 127, 3023, doi: [10.1086/383558](https://doi.org/10.1086/383558)
- Sheppard, S. S., & Jewitt, D. C. 2002, *AJ*, 124, 1757, doi: [10.1086/341954](https://doi.org/10.1086/341954)
- Sheppard, S. S., Lacerda, P., & Ortiz, J. L. 2008, in *The Solar System Beyond Neptune*, ed. M. A. Barucci, H. Boehnhardt, D. P. Cruikshank, A. Morbidelli, & R. Dotson (University of Arizona Press, Tucson), 129
- Showalter, M. R., Benecchi, S. D., Buie, M. W., et al. 2021, *Icarus*, 356, 114098, doi: [10.1016/j.icarus.2020.114098](https://doi.org/10.1016/j.icarus.2020.114098)
- Szabó, G. M., Pál, A., Kiss, C., et al. 2017, *A&A*, 599, A44, doi: [10.1051/0004-6361/201629401](https://doi.org/10.1051/0004-6361/201629401)
- Szabó, G. M., Kiss, C., Szakáts, R., et al. 2020, *ApJS*, 247, 34, doi: [10.3847/1538-4365/ab6b23](https://doi.org/10.3847/1538-4365/ab6b23)
- Szabó, R., Sárneczky, K., Szabó, G. M., et al. 2015, *AJ*, 149, 112, doi: [10.1088/0004-6256/149/3/112](https://doi.org/10.1088/0004-6256/149/3/112)
- Szabó, R., Pál, A., Sárneczky, K., et al. 2016, *A&A*, 596, A40, doi: [10.1051/0004-6361/201629059](https://doi.org/10.1051/0004-6361/201629059)
- Thirouin, A., Noll, K. S., Ortiz, J. L., & Morales, N. 2014, *A&A*, 569, A3, doi: [10.1051/0004-6361/201423567](https://doi.org/10.1051/0004-6361/201423567)
- Thirouin, A., Ortiz, J. L., Campo Bagatin, A., et al. 2012, *MNRAS*, 424, 3156, doi: [10.1111/j.1365-2966.2012.21477.x](https://doi.org/10.1111/j.1365-2966.2012.21477.x)
- Thirouin, A., Ortiz, J. L., Duffard, R., et al. 2010, *A&A*, 522, A93, doi: [10.1051/0004-6361/200912340](https://doi.org/10.1051/0004-6361/200912340)
- Thirouin, A., & Sheppard, S. S. 2018a, *AJ*, 155, 248, doi: [10.3847/1538-3881/aac0ff](https://doi.org/10.3847/1538-3881/aac0ff)
- . 2018b, *AJ*, 155, 248, doi: [10.3847/1538-3881/aac0ff](https://doi.org/10.3847/1538-3881/aac0ff)
- . 2019a, *AJ*, 157, 228, doi: [10.3847/1538-3881/ab18a9](https://doi.org/10.3847/1538-3881/ab18a9)
- . 2019b, *AJ*, 157, 228, doi: [10.3847/1538-3881/ab18a9](https://doi.org/10.3847/1538-3881/ab18a9)
- Vara-Lubiano, M., Benedetti-Rossi, G., Santos-Sanz, P., et al. 2022, arXiv e-prints, arXiv:2205.12878. <https://arxiv.org/abs/2205.12878>
- Vernazza, P., Jorda, L., Ševeček, P., et al. 2020, *Nature Astronomy*, 4, 136, doi: [10.1038/s41550-019-0915-8](https://doi.org/10.1038/s41550-019-0915-8)
- Vernazza, P., Ferrais, M., Jorda, L., et al. 2021, *A&A*, 654, A56, doi: [10.1051/0004-6361/202141781](https://doi.org/10.1051/0004-6361/202141781)
- Vilenius, E., Kiss, C., Müller, T., et al. 2014, *A&A*, 564, A35, doi: [10.1051/0004-6361/201322416](https://doi.org/10.1051/0004-6361/201322416)
- Warner, B. D., Harris, A. W., & Pravec, P. 2009, *Icarus*, 202, 134, doi: [10.1016/j.icarus.2009.02.003](https://doi.org/10.1016/j.icarus.2009.02.003)

APPENDIX

A. BASIC TABLES OF K2 TNO OBSERVATIONS

Table 4 summarises the main circumstances of the K2 observations of our targets, including start and end dates, length, duty, heliocentric and observer range, and phase angle.

Table 4. Transneptunian objects observed by K2, studied in this work, ordered by asteroid number and provisional designation. The columns are: (1) number, name and/or designation of the target; (2) K2 campaign; (3-4) start and end date in Julian Date; (5) the length of observations (day); (6) the number of frames considered in the analysis; (7) the duty cycle of the observations (ratio of useful cadences and all cadences over the time span of the observations); (8) r_h : range of heliocentric distance during the observations (au); (9) Δ : observer – target distance (au); (10) α : phase angle (deg);

| Name (1) | Cam. (2) | Start (3) | End (4) | Length (5) | #frame (6) | Duty (7) | r (8) | Δ (9) | α (10) |
|---------------------------------|-------------|--------------|------------|---------------|---------------|-------------|-----------------|-----------------|------------------|
| (026375) 1999 DE ₉ | C10 | 7584.098 | 7651.713 | 67.6148 | 2549 | 0.770 | 38.426...38.490 | 37.903...39.017 | 1.331...1.563 |
| (035671) 1998 SN ₁₆₅ | C08 | 7418.913 | 7448.930 | 30.0170 | 1424 | 0.969 | 37.479...37.483 | 37.060...37.572 | 1.351...1.495 |
| (066652) Borasisi | C12 | 7738.372 | 7816.653 | 78.2811 | 1222 | 0.319 | 42.013...42.030 | 41.235...42.498 | 0.847...1.332 |
| (080806) 2000 CM ₁₀₅ | C14 | 7905.723 | 7984.903 | 79.1802 | 1469 | 0.379 | 42.795...42.808 | 42.014...43.209 | 0.888...1.401 |
| (119878) 2002 CY ₂₂₄ | C14 | 7942.708 | 7946.999 | 4.2910 | 161 | 0.766 | 38.779...38.782 | 38.508...38.577 | 1.489...1.514 |
| (126154) 2001 YH ₁₄₀ | C05 | 7139.606 | 7214.434 | 74.8278 | 2233 | 0.609 | 36.858...36.871 | 36.179...37.344 | 1.171...1.610 |
| (127871) 2003 FC ₁₂₈ | C10 | 7582.607 | 7630.196 | 47.5899 | 1452 | 0.623 | 33.763...33.774 | 33.172...33.926 | 1.474...1.780 |
| (135182) 2001 QT ₃₂₂ | C08 | 7415.092 | 7443.168 | 28.0758 | 1099 | 0.799 | 37.144...37.145 | 36.733...37.214 | 1.372...1.508 |
| (138537) 2000 OK ₆₇ | C12 | 7767.061 | 7798.038 | 30.9773 | 1195 | 0.788 | 40.087...40.088 | 39.646...40.174 | 1.256...1.395 |
| (145480) 2005 TB ₁₉₀ | C12 | 7767.551 | 7796.403 | 28.8522 | 473 | 0.335 | 46.197...46.198 | 45.789...46.284 | 1.108...1.211 |
| (149348) 2002 VS ₁₃₀ | C13 | 7848.918 | 7879.711 | 30.7934 | 951 | 0.631 | 42.706...42.715 | 42.316...42.837 | 1.224...1.346 |
| (160147) 2001 KN ₇₆ | C15 | 7989.440 | 8077.406 | 87.9667 | 2091 | 0.485 | 39.958...39.964 | 39.125...40.432 | 0.910...1.479 |
| (182934) 2002 GJ ₃₂ | C15 | 8022.910 | 8039.461 | 16.5512 | 678 | 0.836 | 44.365...44.370 | 43.975...44.243 | 1.251...1.328 |
| (307463) 2002 VU ₁₃₀ | C13 | 7852.698 | 7870.802 | 18.1042 | 824 | 0.929 | 40.299...40.309 | 39.927...40.216 | 1.306...1.421 |
| (308379) 2005 RS ₄₃ | C08 | 7426.841 | 7457.206 | 30.3643 | 1386 | 0.932 | 43.256...43.270 | 42.852...43.382 | 1.180...1.298 |
| (307616) 2003 QW ₉₀ | C08 | 7415.072 | 7444.823 | 29.7513 | 1349 | 0.926 | 43.560...43.566 | 43.153...43.657 | 1.167...1.286 |
| (312645) 2010 EP ₆₅ | C17 | 8179.574 | 8246.412 | 66.8383 | 2438 | 0.745 | 33.103...33.109 | 32.319...33.369 | 1.093...1.699 |
| (385266) 2001 QB ₂₉₈ | C12 | 7760.931 | 7786.003 | 25.0720 | 843 | 0.686 | 39.975...39.980 | 39.540...39.972 | 1.269...1.400 |
| (385437) 2003 GH ₅₅ | C15 | 8011.120 | 8050.740 | 39.6208 | 1372 | 0.707 | 41.051...41.055 | 40.554...41.197 | 1.289...1.444 |
| (408832) 2001 QJ ₂₉₈ | C12 | 7761.768 | 7783.203 | 21.4348 | 651 | 0.620 | 44.708...44.710 | 44.328...44.691 | 1.163...1.252 |
| (420356) Praamzius | C16 | 8095.469 | 8100.394 | 4.9245 | 175 | 0.726 | 43.026...43.026 | 43.516...43.585 | 1.100...1.153 |
| (469420) 2001 XP ₂₅₄ | C16 | 8095.469 | 8173.710 | 78.2403 | 2465 | 0.643 | 33.068...33.072 | 32.336...33.574 | 1.129...1.711 |
| (469420) 2001 XP ₂₅₄ | C18 | 8251.541 | 8300.541 | 48.9998 | 1667 | 0.695 | 33.077...33.080 | 32.293...32.995 | 1.105...1.789 |
| (469421) 2001 XD ₂₅₅ | C16 | 8114.738 | 8139.749 | 25.0107 | 356 | 0.291 | 38.794...38.802 | 38.479...38.914 | 1.381...1.461 |
| (469505) 2003 FE ₁₂₈ | C15 | 7989.440 | 8077.447 | 88.0075 | 2723 | 0.632 | 36.081...36.095 | 35.243...36.569 | 1.010...1.638 |
| (469704) 2005 EZ ₂₉₆ | C17 | 8179.533 | 8246.596 | 67.0631 | 2299 | 0.700 | 34.143...34.157 | 33.377...34.458 | 1.109...1.647 |
| (470523) 2008 CS ₁₉₀ | C14 | 7936.251 | 7973.890 | 37.6387 | 1299 | 0.705 | 37.049...37.061 | 36.600...37.211 | 1.456...1.620 |
| (471137) 2010 ET ₆₅ | C10 | 7583.301 | 7651.120 | 67.8191 | 2173 | 0.654 | 39.661...39.666 | 39.069...40.127 | 1.251...1.515 |
| (471150) 2010FC ₄₉ | C10 | 7582.586 | 7651.713 | 69.1269 | 2557 | 0.755 | 39.675...39.684 | 39.104...40.164 | 1.263...1.515 |
| (471318) 2011 JF ₃₁ | C15 | 7990.032 | 8070.827 | 80.7945 | 2675 | 0.676 | 42.199...42.227 | 41.401...42.648 | 0.930...1.403 |
| (472235) 2014 GE ₄₅ | C17 | 8202.930 | 8213.841 | 10.9115 | 413 | 0.773 | 33.709...33.714 | 33.444...33.636 | 1.625...1.668 |
| (508869) 2002 VT ₁₃₀ | C13 | 7853.720 | 7883.144 | 29.4244 | 447 | 0.310 | 43.071...43.073 | 42.712...43.207 | 1.234...1.337 |
| (523658) 2012 DW ₉₈ | C17 | 8179.533 | 8246.535 | 67.0018 | 2193 | 0.668 | 39.725...39.726 | 38.928...39.980 | 0.895...1.415 |
| (523687) 2014 DF ₁₄₃ | C17 | 8179.533 | 8219.665 | 40.1316 | 1579 | 0.803 | 42.937...42.942 | 42.555...43.237 | 1.224...1.310 |
| (523692) 2014 EZ ₅₁ | C15 | 7989.440 | 8077.059 | 87.6193 | 3044 | 0.709 | 55.777...55.819 | 54.970...56.226 | 0.634...1.059 |
| (523698) 2014 GD ₅₄ | C17 | 8179.533 | 8246.474 | 66.9405 | 2696 | 0.822 | 34.763...34.776 | 33.992...35.033 | 1.052...1.618 |
| (523706) 2014 HF ₂₀₀ | C15 | 8028.182 | 8050.781 | 22.5996 | 769 | 0.695 | 37.327...37.339 | 36.963...37.316 | 1.494...1.581 |

Table 4 continued

Table 4 (continued)

| Name | Cam. | Start | End | Length | #frame | Duty | r | Δ | α |
|---------------------------------|------|----------|----------|---------|--------|-------|-----------------|-----------------|---------------|
| (1) | (2) | (3) | (4) | (5) | (6) | (7) | (8) | (9) | (10) |
| (523769) 2014 WS ₅₁₀ | C16 | 8095.469 | 8173.710 | 78.2403 | 2215 | 0.578 | 40.646...40.711 | 40.004...41.189 | 0.962...1.390 |
| (523769) 2014 WS ₅₁₀ | C18 | 8257.222 | 8295.269 | 38.0474 | 1361 | 0.730 | 40.781...40.812 | 40.031...40.598 | 0.957...1.421 |
| (525462) 2005 EO ₃₀₄ | C17 | 8179.840 | 8246.596 | 66.7566 | 1372 | 0.420 | 43.055...43.062 | 42.301...43.378 | 0.896...1.307 |
| (533207) 2014 DJ ₁₄₃ | C15 | 8017.066 | 8037.479 | 20.4132 | 915 | 0.915 | 37.366...37.367 | 36.901...37.218 | 1.440...1.575 |
| (533562) 2014 JQ ₈₀ | C15 | 8017.597 | 8048.043 | 30.4461 | 700 | 0.469 | 31.673...31.683 | 31.177...31.672 | 1.673...1.865 |
| (533676) 2014 LS ₂₈ | C15 | 7989.440 | 8007.380 | 17.9407 | 728 | 0.828 | 42.137...42.140 | 41.327...41.544 | 0.907...1.177 |
| (535018) 2014 WA ₅₀₉ | C14 | 7916.553 | 7923.521 | 6.9679 | 298 | 0.873 | 42.744...42.745 | 42.033...42.117 | 1.002...1.104 |
| (535023) 2014 WO ₅₀₉ | C14 | 7905.723 | 7984.535 | 78.8124 | 2159 | 0.559 | 39.933...39.934 | 39.100...40.248 | 0.857...1.503 |
| (535028) 2014 WA ₅₁₀ | C14 | 7905.723 | 7984.985 | 79.2619 | 1986 | 0.512 | 45.224...45.232 | 44.382...45.540 | 0.739...1.327 |
| (535030) 2014 WJ ₅₁₀ | C14 | 7929.855 | 7970.314 | 40.4585 | 1511 | 0.762 | 34.845...34.848 | 34.337...34.981 | 1.494...1.722 |
| (535228) 2014 YE ₅₀ | C18 | 8267.970 | 8297.599 | 29.6287 | 1169 | 0.806 | 47.853...47.880 | 47.346...47.842 | 1.058...1.236 |
| (535231) 2014 YJ ₅₀ | C16 | 8111.428 | 8134.273 | 22.8448 | 449 | 0.401 | 35.254...35.265 | 35.057...35.432 | 1.569...1.608 |
| 2014 AM ₅₅ | C16 | 8095.490 | 8173.710 | 78.2198 | 2426 | 0.633 | 48.222...48.249 | 47.529...48.813 | 0.829...1.171 |
| 2013 AP ₁₈₃ | C16 | 8121.665 | 8163.677 | 42.0115 | 1272 | 0.618 | 47.635...47.672 | 47.063...47.709 | 0.929...1.188 |
| 2013 AT ₁₈₃ | C16 | 8095.551 | 8173.812 | 78.2607 | 2177 | 0.568 | 62.520...62.591 | 61.813...62.971 | 0.549...0.906 |
| 2013 AT ₁₈₃ | C18 | 8251.541 | 8289.486 | 37.9452 | 1389 | 0.747 | 62.662...62.696 | 61.920...62.496 | 0.623...0.923 |
| 2015 BB ₅₁₉ | C18 | 8261.922 | 8301.277 | 39.3551 | 1454 | 0.754 | 42.844...42.881 | 42.312...42.976 | 1.158...1.380 |
| 2015 BC ₅₁₉ | C16 | 8114.902 | 8134.395 | 19.4937 | 734 | 0.769 | 36.020...36.035 | 35.774...36.121 | 1.523...1.575 |
| 2015 BC ₅₁₉ | C18 | 8262.269 | 8288.056 | 25.7872 | 895 | 0.709 | 35.895...35.916 | 35.344...35.713 | 1.343...1.619 |
| 2015 BZ ₅₁₈ | C15 | 7989.685 | 8077.427 | 87.7419 | 1204 | 0.280 | 48.805...48.843 | 48.091...49.385 | 0.861...1.215 |
| 2015 DA ₂₂₅ | C18 | 8265.048 | 8299.519 | 34.4715 | 950 | 0.563 | 36.545...36.560 | 35.998...36.518 | 1.332...1.622 |
| 2013 FA ₂₈ | C17 | 8179.533 | 8246.596 | 67.0631 | 2061 | 0.627 | 44.919...44.926 | 44.162...45.239 | 0.854...1.253 |
| 2014 GJ ₅₄ | C15 | 8014.144 | 8045.182 | 31.0387 | 720 | 0.474 | 29.815...29.829 | 29.332...29.812 | 1.779...1.986 |
| 2001 HZ ₅₈ | C15 | 7989.440 | 8077.447 | 88.0075 | 2500 | 0.580 | 43.692...43.698 | 42.857...44.180 | 0.837...1.353 |
| 2013 JV ₆₅ | C15 | 7989.440 | 8077.427 | 87.9871 | 2160 | 0.501 | 41.570...41.576 | 40.776...42.095 | 0.940...1.424 |
| 2003 QA ₉₂ | C12 | 7757.968 | 7786.105 | 28.1371 | 708 | 0.514 | 37.031...37.035 | 36.591...37.063 | 1.365...1.512 |
| 2001 QX ₂₉₇ | C12 | 7760.134 | 7786.105 | 25.9711 | 1029 | 0.809 | 43.238...43.240 | 42.803...43.243 | 1.171...1.295 |
| 2004 TF ₂₈₂ | C13 | 7842.951 | 7871.538 | 28.5866 | 809 | 0.578 | 40.791...40.805 | 40.382...40.869 | 1.266...1.405 |
| 2004 TV ₃₅₇ | C13 | 7856.682 | 7872.294 | 15.6113 | 613 | 0.802 | 35.017...35.021 | 34.853...35.113 | 1.606...1.636 |
| 2004 XR ₁₉₀ | C13 | 7856.315 | 7885.473 | 29.1588 | 796 | 0.557 | 57.336...57.343 | 57.025...57.503 | 0.942...1.005 |
| 2001 XU ₂₅₄ | C16 | 8095.469 | 8173.812 | 78.3424 | 1778 | 0.463 | 41.552...41.566 | 40.756...41.995 | 0.794...1.365 |
| 2009 YG ₁₉ | C13 | 7847.508 | 7856.192 | 8.6843 | 412 | 0.969 | 34.810...34.815 | 34.390...34.529 | 1.482...1.571 |
| 2003 YS ₁₇₉ | C16 | 8097.881 | 8169.092 | 71.2111 | 542 | 0.155 | 43.490...43.495 | 42.761...43.900 | 0.869...1.304 |

Table 5 lists the main orbital elements obtained from the JPL Horizons service (Giorgini et al. 1996), as well as the dynamical group or mean motion resonance of the target, the R-band (Kepler) absolute magnitudes obtained in this work (see Sect. 3.1), and the estimated diameters of our targets. These latter are radiometric size estimates, typically obtained from Herschel and Spitzer thermal infrared emission measurements, whenever they are available (Lellouch et al. 2013; Vilenius et al. 2014; Farkas-Takács et al. 2020). When no radiometric size estimate was found we used the H_V absolute magnitude of the object (also listed in Table 5), assuming a geometric albedo of $p_V = 0.12$ for cold classicals which are predominantly red objects with relatively high albedos, while we used $p_V = 0.08$ for all other dynamical groups (Lacerda et al. 2014; Farkas-Takács et al. 2020). The diameter is calculated as: $D(\text{km}) = 1329 p_V^{-1/2} 10^{-0.2H_V}$.

Table 5. Summary table of the main orbital characteristics and dynamical classification of our targets. The columns are: (1) name and/or provisional designation; (2) V-band absolute magnitude (mag); (3) semi-major axis (au); (4) eccentricity; (5) inclination (deg); (6) dynamical class or mean-motion resonance with Neptune. Cold and hot classicals are separated by the inclination $i = 4^\circ.5$ (see e.g. Gladman et al. 2008); (7) phase-angle-uncorrected mean absolute brightness (Kepler \approx R-band, mag); (8) mean phase angle (deg); (9) phase-angle-corrected mean absolute brightness (Kepler \approx R-band, mag). (10) estimated diameter (km), superscript letters mark targets with estimates based on radiometric data: a – Lellouch et al. (2013), b – Vilenius et al. (2014) c – Farkas-Takács et al. (2020). Diameters of unmarked targets are estimated using their H_V absolute magnitudes (see the text for details).

| Name | H_V | a | e | i | Dynamical group | $\langle m_{11}^R(\alpha) \rangle$ | $\langle \alpha \rangle$ | $m_{110}^R(\alpha)$ | D |
|------------------------|-------|------------|-----------|----------|-----------------|------------------------------------|--------------------------|---------------------|-------------------|
| (1) | (2) | (3) | (4) | (5) | (6) | (7) | (8) | (9) | (10) |
| 1998 SN ₁₆₅ | 5.68 | 37.8239563 | 0.0399826 | 4.61245 | hot classical | 5.24 | 1.45 | 5.23±0.02 | 393 ^b |
| 1999 DE ₉ | 4.94 | 55.5040117 | 0.4168371 | 7.62938 | 2:5 resonance | 4.45 | 1.49 | 4.20±0.06 | 311 ^a |
| 2000 CM ₁₀₅ | 6.68 | 42.1255750 | 0.0640919 | 3.75516 | cold classical | 6.75 | 1.18 | 6.54±0.16 | 176 |
| 2000 OK ₆₇ | 6.0 | 46.5813354 | 0.1403453 | 4.88465 | hot classical | 6.56 | 1.35 | 6.32±0.18 | 296 |
| 2001 HZ ₅₈ | 6.6 | 43.0180466 | 0.0323816 | 2.93273 | cold classical | 6.55 | 1.20 | 6.35±0.16 | 183 |
| 2001 KN ₇₆ | 6.6 | 44.0637410 | 0.0956953 | 2.64496 | cold classical | 7.08 | 1.30 | 6.85±0.17 | 182 |
| 2001 QB ₂₉₈ | 6.8 | 42.7192221 | 0.0995969 | 1.79485 | cold classical | 6.62 | 1.35 | 6.38±0.18 | 167 |
| 2001 QJ ₂₉₈ | 6.2 | 44.1753883 | 0.0365290 | 2.15477 | cold classical | 5.82 | 1.22 | 5.61±0.16 | 220 |
| 2001 QT ₃₂₂ | 6.2 | 37.0258514 | 0.0220311 | 1.84662 | inner classical | 7.62 | 1.47 | 7.37±0.20 | 270 |
| 2001 QX ₂₉₇ | 6.3 | 44.2115741 | 0.0270365 | 0.90745 | cold classical | 6.66 | 1.25 | 6.45±0.17 | 210 |
| 2001 XD ₂₅₅ | 5.8 | 39.2882985 | 0.1118632 | 18.14109 | plutino | 5.99 | 1.44 | 5.74±0.19 | 325 |
| 2001 XP ₂₅₄ | 7.77 | 42.0465415 | 0.2142201 | 2.61611 | 3:5 resonance | 7.51 | 1.52 | 7.25±0.20 | 131 |
| 2001 XU ₂₅₄ | 6.68 | 43.2829795 | 0.0780917 | 6.52230 | hot classical | 6.38 | 1.18 | 6.18±0.16 | 217 |
| 2001 YH ₁₄₀ | 5.58 | 42.1828001 | 0.1369339 | 11.09996 | 3:5 resonance | 5.75 | 1.50 | 5.49±0.20 | 252 ^c |
| 2002 CY ₂₂₄ | 6.16 | 53.7570643 | 0.3432009 | 15.76009 | 5:12 resonance | 7.27 | 1.50 | 7.01±0.22 | <220 ^c |
| 2002 GJ ₃₂ | 5.4 | 44.5446573 | 0.1073526 | 11.57225 | hot classical | 6.11 | 1.30 | 5.89±0.17 | 224 ^a |
| 2002 VS ₁₃₀ | 6.3 | 44.8124374 | 0.1201659 | 3.00131 | cold classical | 6.09 | 1.31 | 5.86±0.17 | 209 |
| 2002 VT ₁₃₀ | 5.7 | 42.2145036 | 0.0356054 | 1.16426 | cold classical | 5.43 | 1.30 | 5.21±0.17 | 277 |
| 2002 VU ₁₃₀ | 5.9 | 38.9541796 | 0.2103117 | 1.37856 | plutino | 5.72 | 1.38 | 5.48±0.18 | 310 |
| 2003 FC ₁₂₈ | 7.41 | 35.0390366 | 0.0839447 | 2.37160 | 4:5 resonance | 6.92 | 1.71 | 6.62±0.23 | 155 |
| 2003 FE ₁₂₈ | 6.37 | 48.4332947 | 0.2592514 | 3.38301 | 1:2 resonance | 6.53 | 1.43 | 6.18±0.46 | 137 ^c |
| 2003 GH ₅₅ | 6.0 | 44.4898956 | 0.0844735 | 1.10267 | cold classical | 6.16 | 1.40 | 6.20±0.64 | 178 ^b |
| 2003 QA ₉₂ | 6.9 | 38.2803717 | 0.0583336 | 3.42715 | inner classical | 6.80 | 1.48 | 6.54±0.20 | 196 |
| 2003 QW ₉₀ | 5.0 | 43.6941429 | 0.0734856 | 10.36787 | hot classical | 4.65 | 1.26 | 4.43±0.17 | 470 |
| 2003 YS ₁₇₉ | 6.8 | 43.4354691 | 0.0266317 | 3.73349 | cold classical | 6.19 | 1.05 | 6.01±0.14 | 167 |
| 2004 TF ₂₈₂ | 6.3 | 79.8663748 | 0.5072393 | 23.23663 | scattered disk | 6.02 | 1.37 | 5.78±0.18 | 258 |
| 2004 TV ₃₅₇ | 6.9 | 47.3800039 | 0.2722973 | 9.78559 | 1:2 resonance | 7.21 | 1.63 | 6.93±0.22 | 196 |
| 2004 XR ₁₉₀ | 4.3 | 57.2561486 | 0.1073786 | 46.79343 | scattered disk | 3.96 | 0.98 | 3.79±0.13 | 649 |
| 2005 EO ₃₀₄ | 6.21 | 45.8983194 | 0.0739658 | 3.41227 | cold classical | 6.16 | 1.23 | 5.95±0.16 | 219 |
| 2005 EZ ₂₉₆ | 7.13 | 39.6766516 | 0.1557282 | 1.77550 | plutino | 7.21 | 1.47 | 6.95±0.19 | 176 |
| 2005 RS ₄₃ | 5.18 | 47.7306105 | 0.2003342 | 10.02598 | 1:2 resonance | 4.76 | 1.27 | 4.54±0.17 | 432 |

Table 5 continued

Table 5 (continued)

| Name | H_V | a | e | i | Dynamical group | $\langle m_{11}^R(\alpha) \rangle$ | $\langle \alpha \rangle$ | $m_{110}^R(\alpha)$ | D |
|------------------------|-------|------------|-----------|----------|-----------------|------------------------------------|--------------------------|---------------------|------------------|
| (1) | (2) | (3) | (4) | (5) | (6) | (7) | (8) | (9) | (10) |
| 2005 TB ₁₉₀ | 4.55 | 75.9529877 | 0.3917797 | 26.49004 | scattered disk | 4.63 | 1.17 | 4.63±0.13 | 507 ^a |
| 2008 CS ₁₉₀ | 6.27 | 42.2933803 | 0.1579361 | 15.94423 | 3:5 resonance | 6.33 | 1.58 | 6.06±0.21 | 262 |
| 2009 YG ₁₉ | 6.2 | 55.2226347 | 0.4040541 | 5.16230 | 2:5 resonance | 5.91 | 1.53 | 5.64±0.20 | 270 |
| 2010 EP ₆₅ | 5.54 | 47.8794282 | 0.3094197 | 18.86373 | 1:2 resonance | 5.55 | 1.55 | 5.29±0.20 | 366 |
| 2010 ET ₆₅ | 5.26 | 62.5104891 | 0.3659258 | 30.58345 | scattered disk | 4.71 | 1.44 | 4.46±0.19 | 417 |
| 2010 FC ₄₉ | 5.88 | 39.0790779 | 0.0535418 | 39.73235 | plutino | 4.49 | 1.45 | 4.24±0.19 | 313 |
| 2011 JF ₃₁ | 5.43 | 41.6753240 | 0.1307786 | 27.64613 | hot classical | 5.50 | 1.26 | 5.28±0.17 | 385 |
| 2012 DW ₉₈ | 6.06 | 41.2840227 | 0.0379671 | 18.99296 | hot classical | 6.12 | 1.28 | 5.90±0.17 | 288 |
| 2013 AP ₁₈₃ | 5.67 | 57.5543033 | 0.3668924 | 3.33318 | 3:8 resonance | 5.41 | 1.10 | 5.22±0.15 | 345 |
| 2013 AT ₁₈₃ | 4.9 | 61.6173083 | 0.4217387 | 28.12567 | scattered disk | 4.82 | 0.81 | 4.68±0.11 | 492 |
| 2013 FA ₂₈ | 6.2 | 44.4091197 | 0.0426125 | 1.53768 | cold classical | 6.22 | 1.14 | 6.02±0.15 | 220 |
| 2013 JV ₆₅ | 6.35 | 42.9996513 | 0.0424042 | 3.21441 | cold classical | 6.23 | 1.29 | 6.01±0.17 | 205 |
| 2014 AM ₅₅ | 5.2 | 47.0230084 | 0.1423797 | 7.18355 | hot classical | 5.14 | 1.06 | 4.94±0.14 | 428 |
| 2014 DF ₁₄₃ | 5.56 | 42.8307595 | 0.0456454 | 23.68086 | hot classical | 5.58 | 1.28 | 5.36±0.17 | 363 |
| 2014 DJ ₁₄₃ | 6.61 | 38.1807753 | 0.0232355 | 6.93181 | 4:13 resonance | 6.76 | 1.52 | 6.50±0.20 | 224 |
| 2014 EZ ₅₁ | 3.92 | 52.5242987 | 0.2263985 | 10.25719 | scattered disk | 4.09 | 0.94 | 3.93±0.12 | 176 |
| 2014 GD ₅₄ | 6.71 | 90.1672371 | 0.6157590 | 4.74239 | scattered disk | 6.78 | 1.47 | 6.52±0.19 | 214 |
| 2014 GE ₄₅ | 6.56 | 56.0228149 | 0.4158196 | 0.80808 | 2:5 resonance | 6.73 | 1.65 | 6.45±0.22 | 229 |
| 2014 GJ ₅₄ | 7.5 | 39.8224386 | 0.2801272 | 17.22611 | plutino | 7.55 | 1.90 | 7.22±0.25 | 149 |
| 2014 HF ₂₀₀ | 5.9 | 61.7601933 | 0.4255242 | 9.71007 | scattered disk | 6.05 | 1.55 | 5.78±0.20 | 310 |
| 2014 JQ ₈₀ | 7.38 | 39.7549394 | 0.2233159 | 7.97258 | plutino | 7.32 | 1.78 | 7.01±0.24 | 157 |
| 2014 LS ₂₈ | 6.2 | 43.6029549 | 0.0681892 | 3.82390 | cold classical | 6.17 | 1.04 | 5.99±0.14 | 220 |
| 2014 WA ₅₀₉ | 6.0 | 44.0261031 | 0.0531885 | 3.00216 | cold classical | 6.13 | 1.06 | 5.95±0.14 | 241 |
| 2014 WA ₅₁₀ | 5.9 | 45.4170544 | 0.0367855 | 2.15623 | cold classical | 5.89 | 1.08 | 5.71±0.14 | 252 |
| 2014 WJ ₅₁₀ | 6.71 | 68.4462110 | 0.4912992 | 24.36183 | scattered disk | 6.69 | 1.67 | 6.41±0.22 | 174 |
| 2014 WO ₅₀₉ | 6.3 | 43.9992014 | 0.0923767 | 3.75719 | cold classical | 6.19 | 1.28 | 5.96±0.17 | 210 |
| 2014 WS ₅₁₀ | 5.55 | 54.9409609 | 0.3708612 | 8.90970 | 2:5 resonance | 5.65 | 1.25 | 5.44±0.16 | 365 |
| 2014 YE ₅₀ | 5.53 | 59.1067258 | 0.3757100 | 26.91854 | scattered disk | 5.42 | 1.17 | 5.22±0.16 | 368 |
| 2014 YJ ₅₀ | 6.84 | 39.3040558 | 0.1951859 | 7.28212 | plutino | 7.13 | 1.60 | 6.86±0.21 | 201 |
| 2015 BB ₅₁₉ | 6.7 | 63.1405090 | 0.4398171 | 27.62710 | scattered disk | 6.59 | 1.32 | 6.37±0.17 | 215 |
| 2015 BC ₅₁₉ | 6.7 | 55.2299967 | 0.4166677 | 1.72294 | 2:5 resonance | 6.94 | 1.52 | 6.68±0.20 | 215 |
| 2015 BZ ₅₁₈ | 4.81 | 47.2750427 | 0.1850024 | 11.35989 | other TNO | 5.00 | 1.03 | 4.82±0.14 | 513 |
| 2015 DA ₂₂₅ | 7.47 | 72.9126980 | 0.5110819 | 27.66698 | scattered disk | 7.32 | 1.51 | 7.06±0.20 | 151 |
| Borasisi | 5.9 | 43.8343021 | 0.0906165 | 0.56342 | cold classical | 5.90 | 1.08 | 5.72±0.14 | 163 ^b |
| Praamzius | 5.75 | 42.5834453 | 0.0104114 | 1.09950 | cold classical | 5.93 | 1.24 | 5.72±0.17 | 270 |

B. INDIVIDUAL OBJECTS WITH DETECTED LIGHT CURVE PERIODS

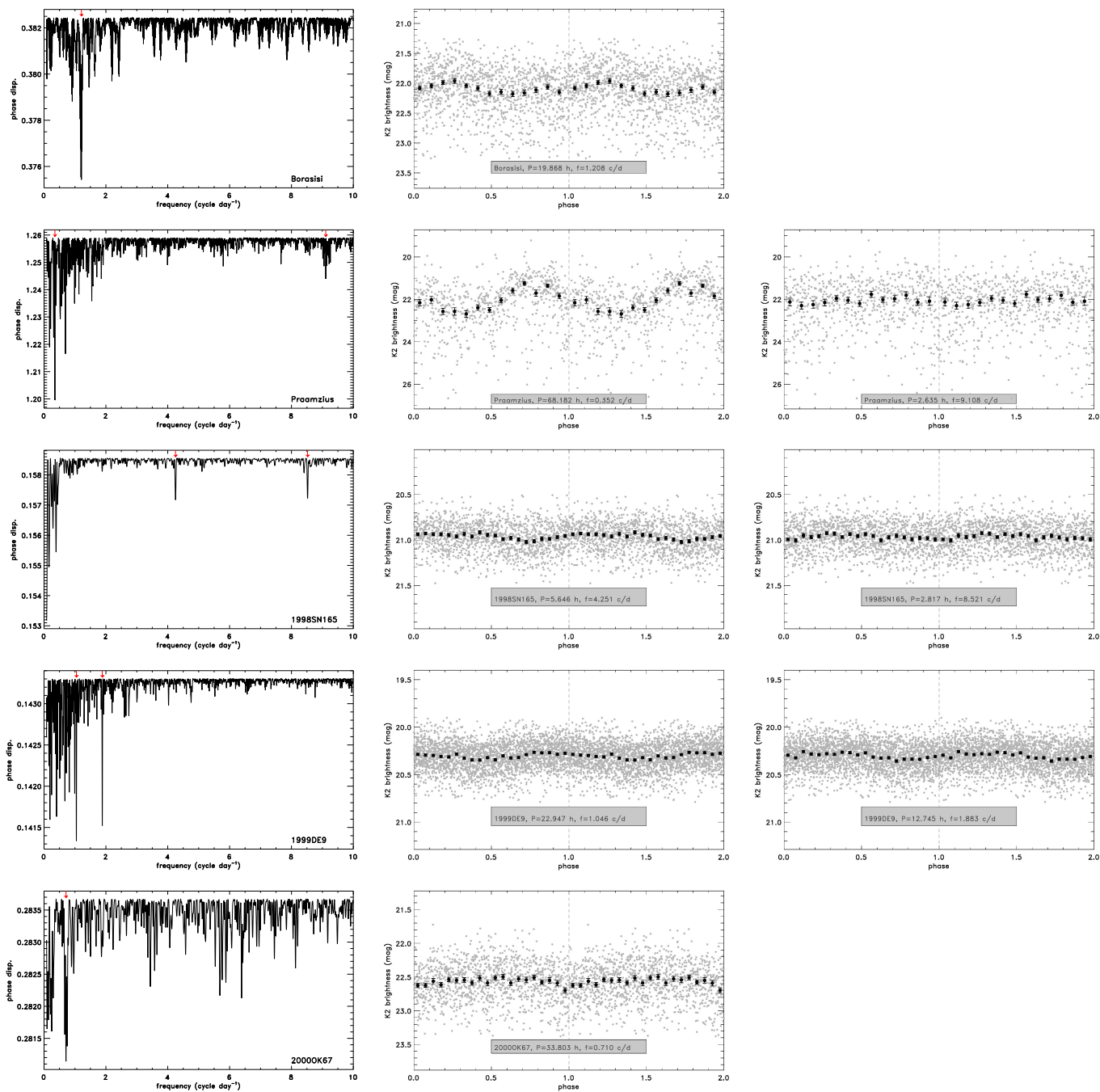


Figure 9. For each target (one target a row) we present the phase dispersion versus frequency on the left column of the figure. Red arrows mark the light curve frequencies detected by our analysis. On the panels to the right we show the light curves folded with the periods/frequencies identified, as listed in Table 1. The name of the target and the folding periods/frequencies are indicated.

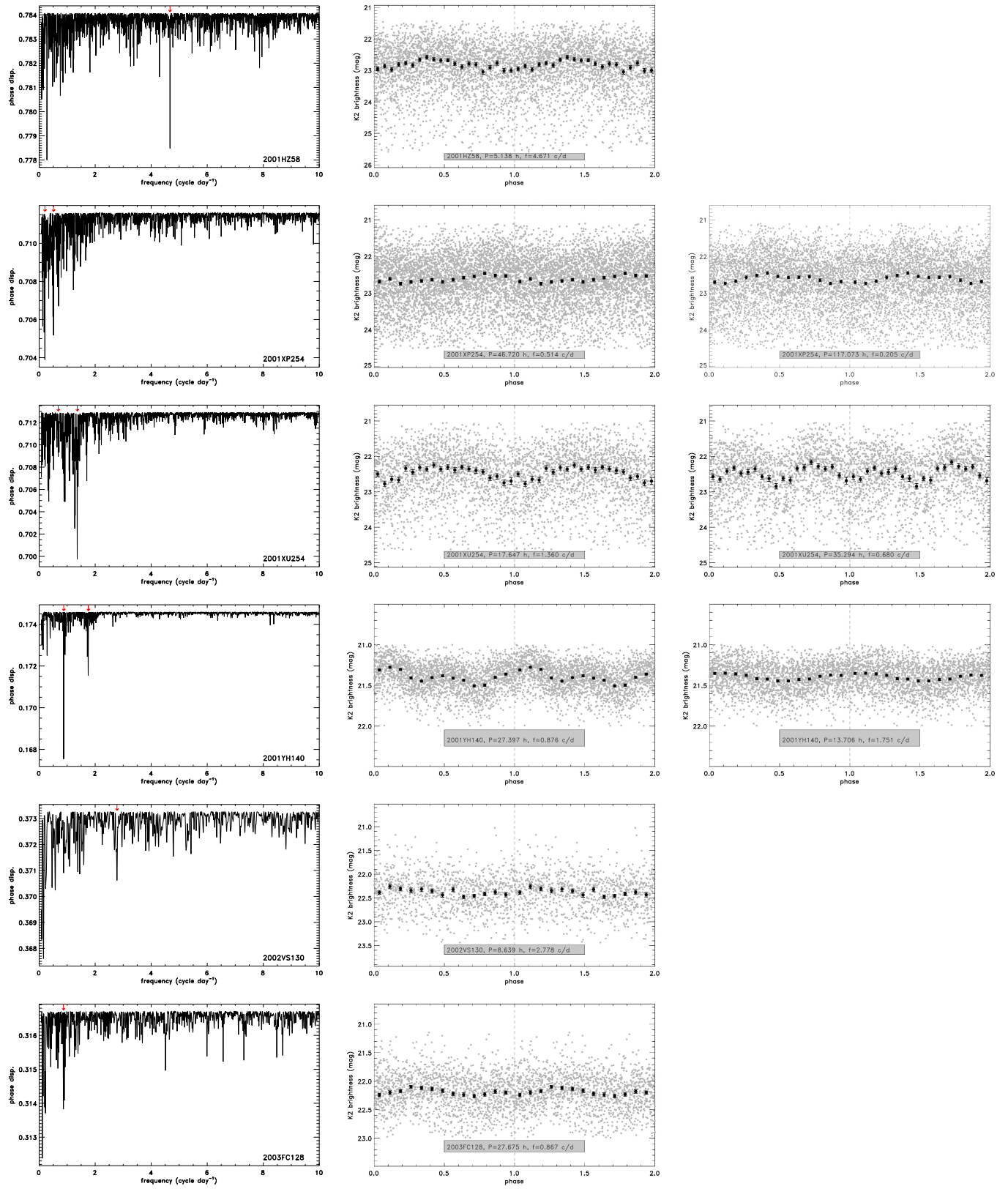


Figure 9.

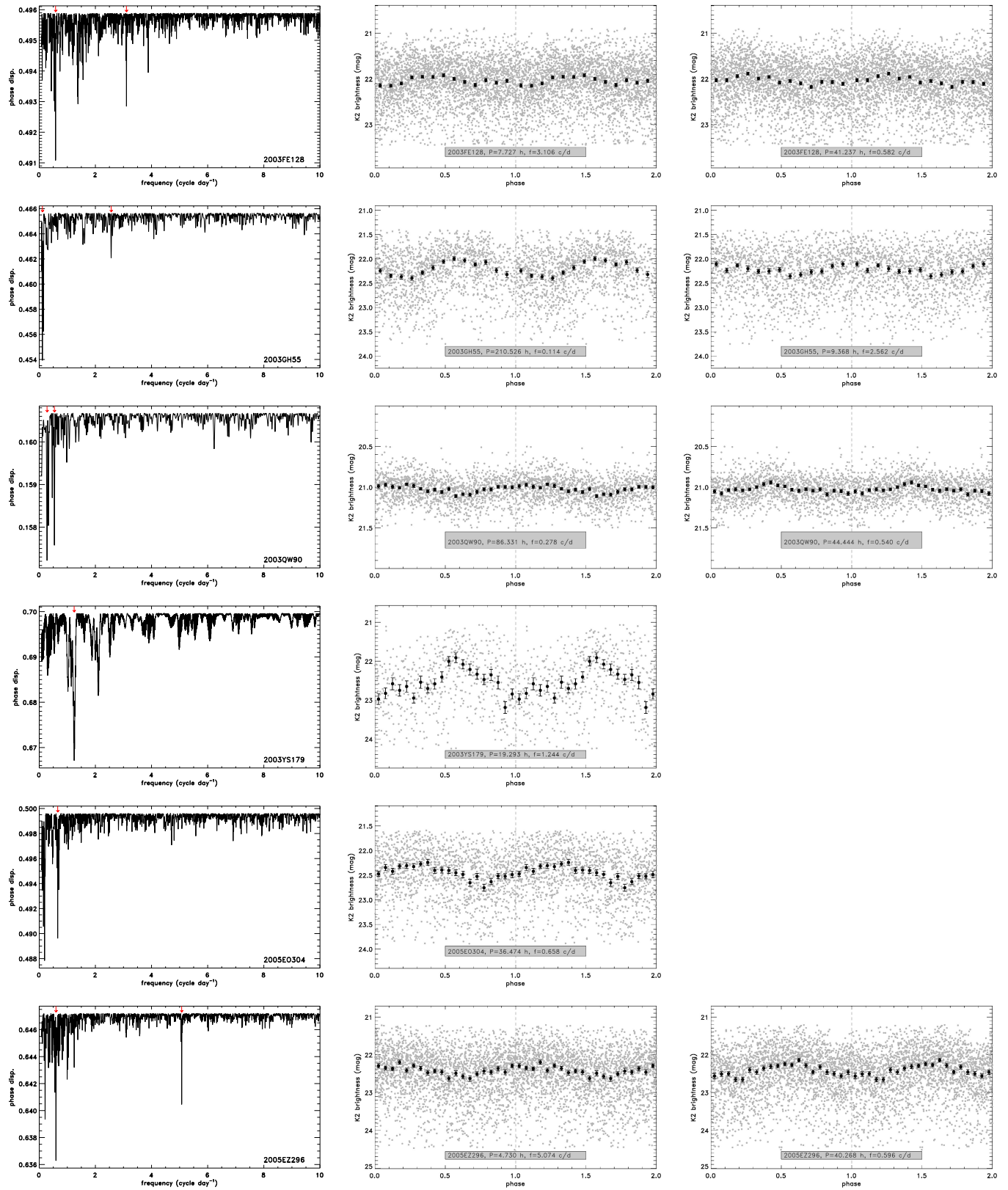


Figure 9.

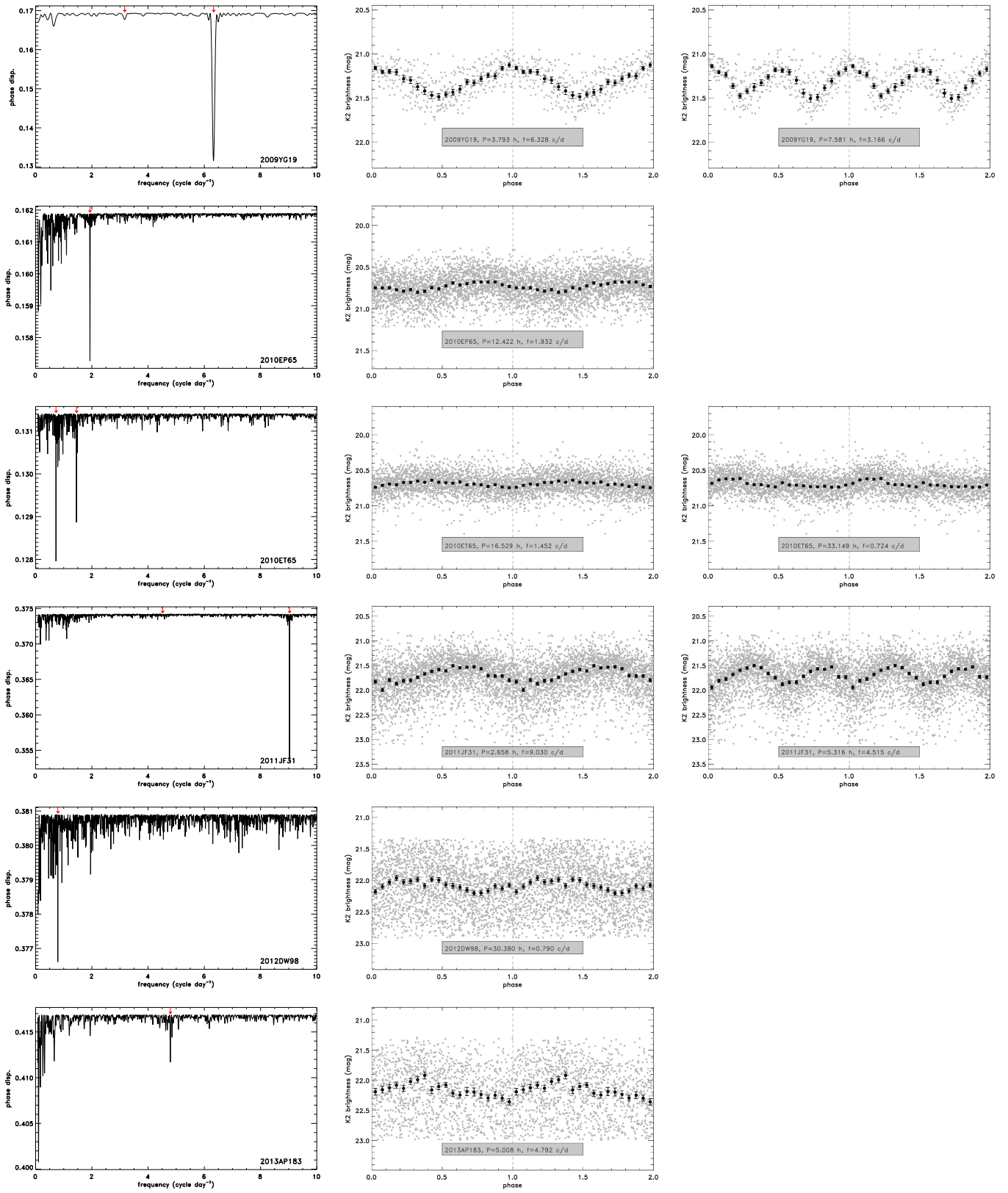


Figure 9.

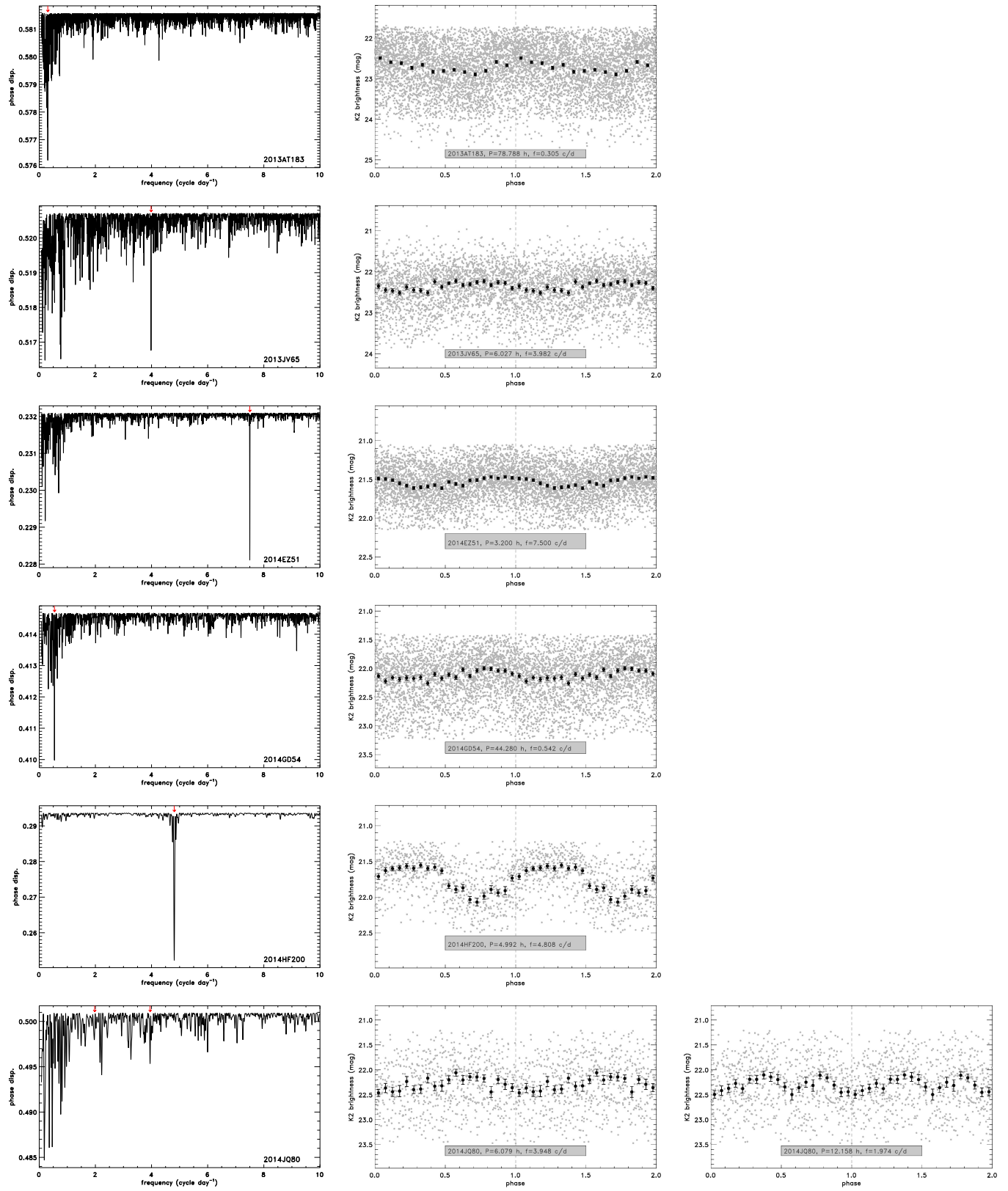


Figure 9.

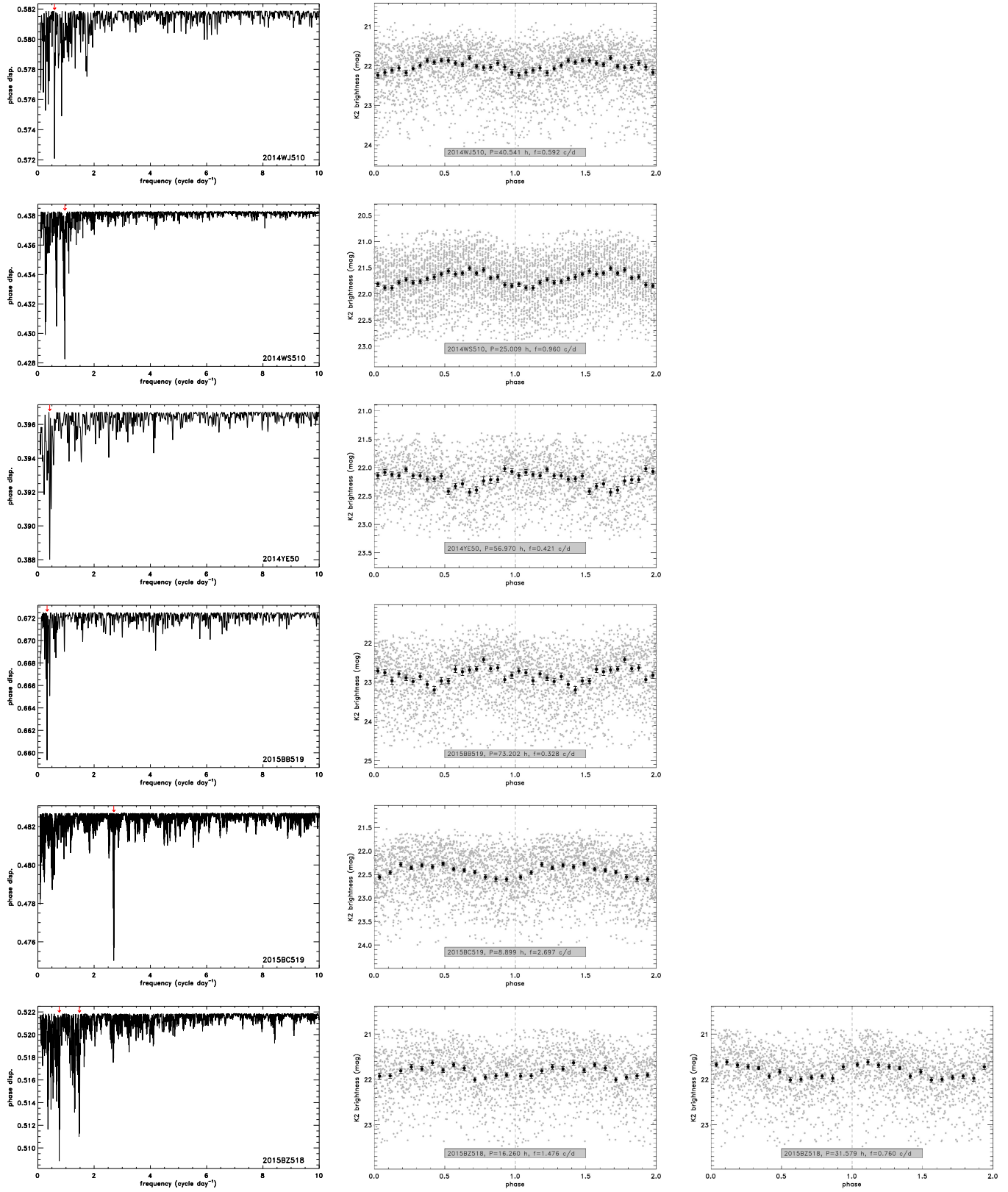


Figure 9.

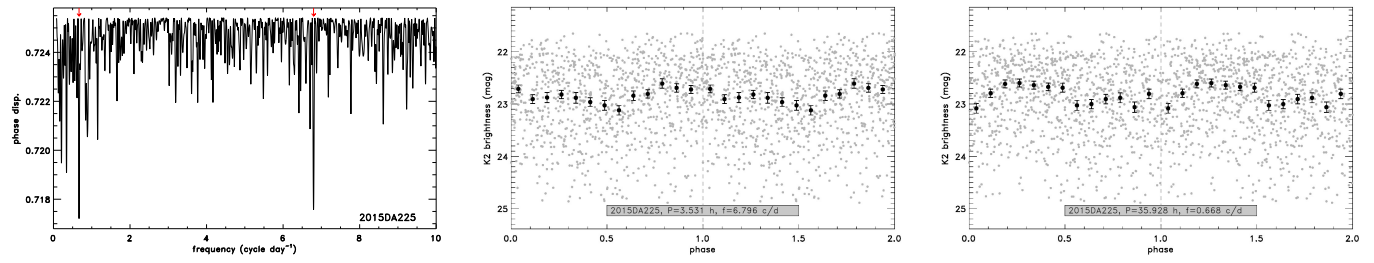


Figure 9.

C. INDIVIDUAL OBJECTS WITHOUT DETECTED LIGHT CURVE PERIODS

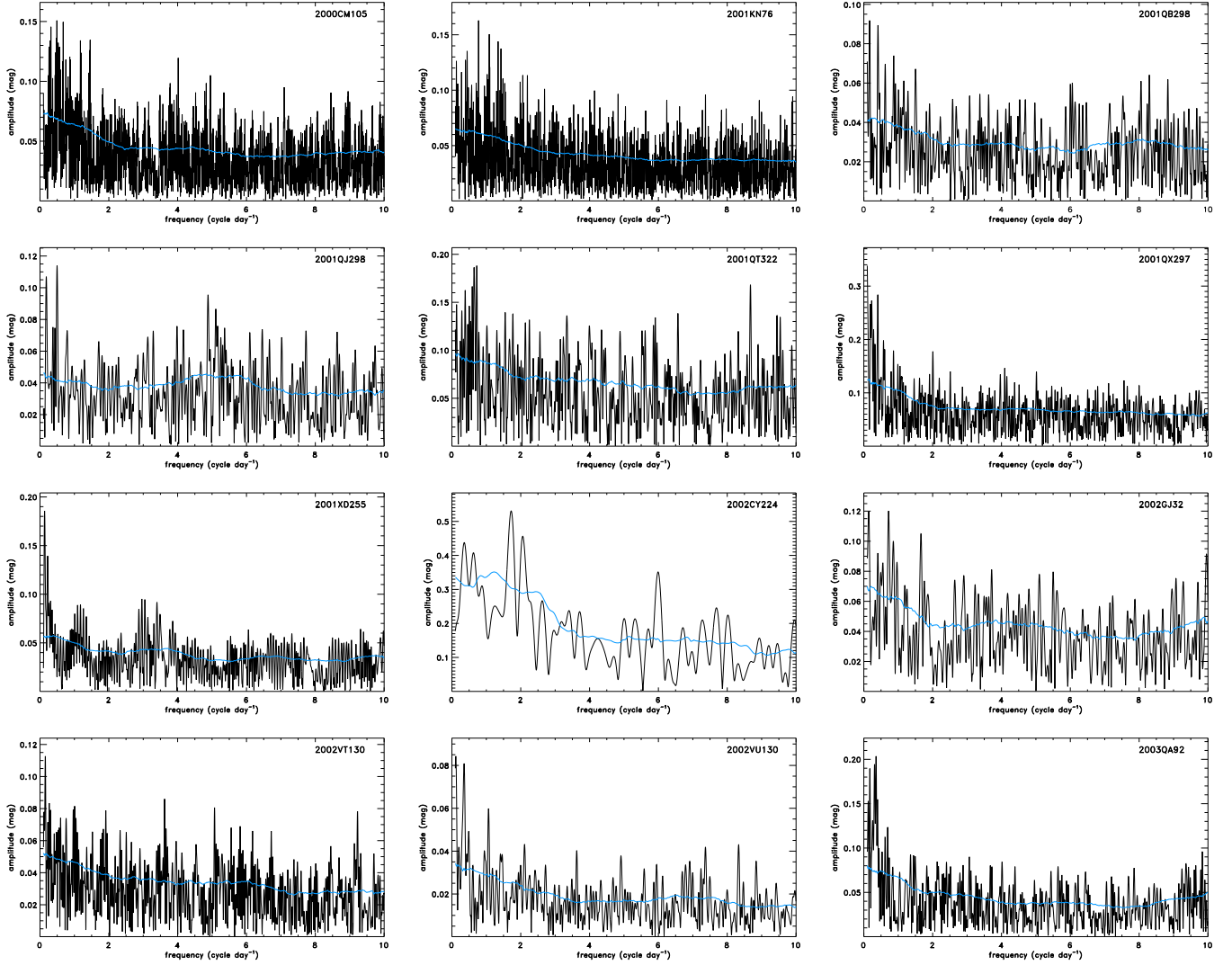


Figure 10. In this figure we present the Fourier spectrum (amplitude vs. frequency) of the light curves of targets for which no peaks in the Fourier/residual spectra matched the detection criteria, as described in Sect. 2.1. The blue curve represents the 1σ r.m.s. of the frequency spectrum. The name of the target is indicated in each figure.

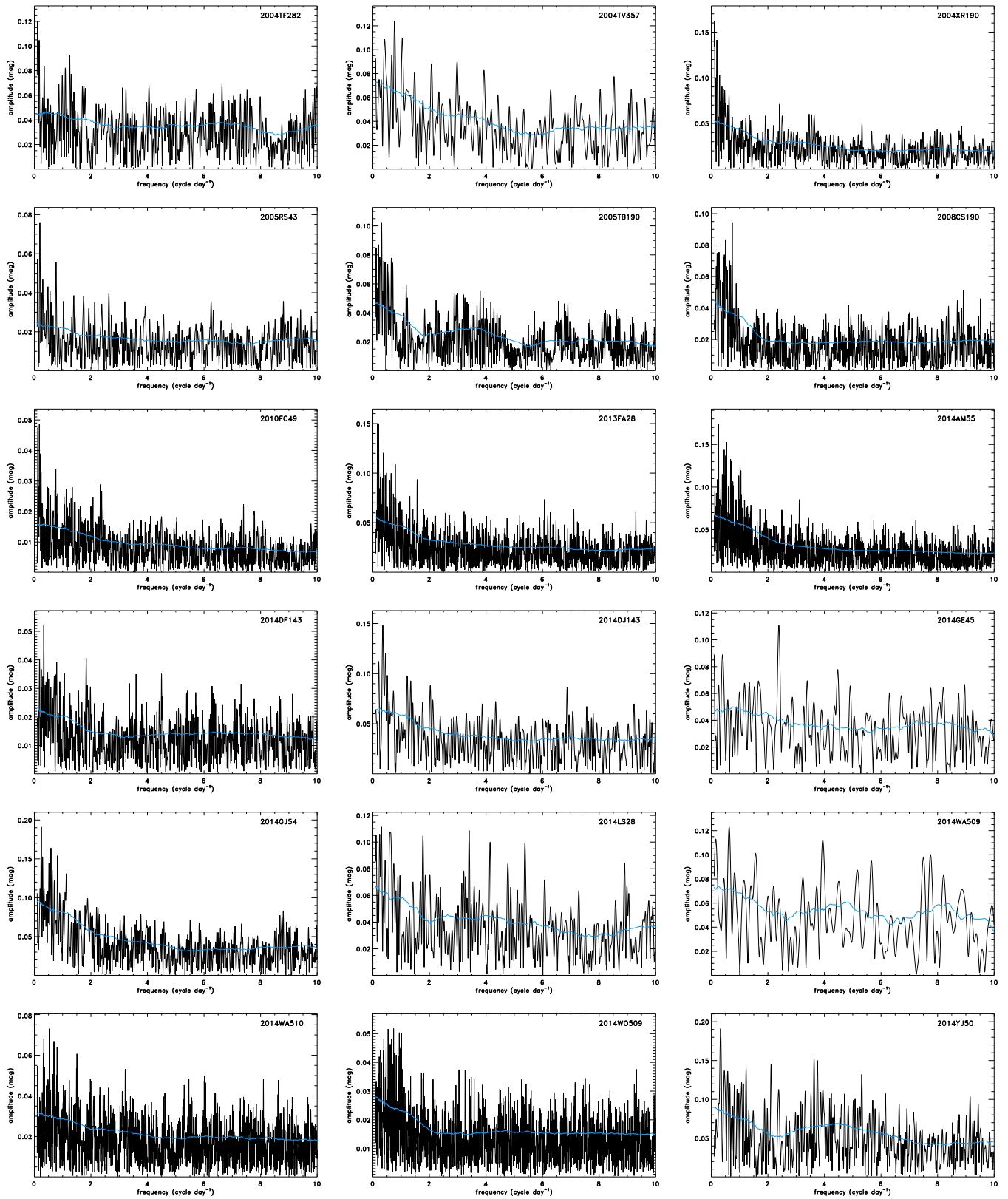


Figure 10.

D. LIGHT CURVE DATA

The data of all light curves presented in this paper are available as a single ASCII data table. Note that all data presented are *uncorrected* for heliocentric/observer distances and phase angle. An example table is shown below.

| Desig. | Name/ID | Camp. | JD | m | δm | R.A. | DEC |
|--------|------------------|-------|---------------|---------|------------|-----------|----------|
| 26375 | (26375) 1999 DE9 | C10 | 2457584.09825 | 20.6242 | 0.1930 | 181.30961 | -6.24154 |
| 26375 | (26375) 1999 DE9 | C10 | 2457584.13911 | 20.5693 | 0.1496 | 181.30934 | -6.24136 |
| 26375 | (26375) 1999 DE9 | C10 | 2457584.15955 | 20.5848 | 0.1296 | 181.30921 | -6.24127 |
| 26375 | (26375) 1999 DE9 | C10 | 2457584.20041 | 20.5265 | 0.1244 | 181.30893 | -6.24108 |
| 26375 | (26375) 1999 DE9 | C10 | 2457584.22085 | 20.3055 | 0.0783 | 181.30880 | -6.24099 |
| 26375 | (26375) 1999 DE9 | C10 | 2457584.24128 | 20.3238 | 0.0911 | 181.30866 | -6.24090 |
| 26375 | (26375) 1999 DE9 | C10 | 2457584.26172 | 20.2942 | 0.1116 | 181.30852 | -6.24080 |
| 26375 | (26375) 1999 DE9 | C10 | 2457584.28215 | 20.3690 | 0.0928 | 181.30839 | -6.24071 |
| 26375 | (26375) 1999 DE9 | C10 | 2457584.30258 | 20.4051 | 0.0982 | 181.30825 | -6.24062 |
| 26375 | (26375) 1999 DE9 | C10 | 2457584.32302 | 20.3264 | 0.1024 | 181.30812 | -6.24053 |

Table 6. Example table presenting the first lines of the ASCII data table of the K2 TNO photometry results. The columns of the table are: (1) identification in Minor Planet Center’s packed designation format^b (characters 1-8); (2) target name or asteroid number, if available, or provisional designation (chars 9-30), in ‘human-readable’ format; (3) Campaign ID; (4) Julian date; (5) K2 brightness (mag); (6) uncertainty of K2 brightness (mag); (7)-(8) R.A. and DEC of the center of the measuring aperture, centered on the target on the K2 image (decimal degrees). These coordinates are taken from the object’s ephemeris provided by NASA’s Horizon system, generated as seen from the Kepler spacecraft at the time of the data reduction. Note that a later refinement in the object’s orbit might result in (slightly) different R.A. and DEC values.

^a <https://www.minorplanetcenter.net/iau/info/PackedDes.html>

^b <https://www.minorplanetcenter.net/iau/info/PackedDes.html>